CHAPTER 5

A SEARCH FOR XUV EMISSION IN LOCAL BCDS

5.1 Motivation

As described in Chapter 2 of this thesis, the discovery and study of spatially extended star formation in galaxies[2, 18, 31, 318, 319, 358, 407] have opened a new window as to how the galactic disks grow and evolve. XUV disks are signatures of inside-out mode of mass assembly, where a galaxy gradually grows its inner regions first and then the outer parts[18, 336]. Incidentally, the inside-out mode is prevalent in the massive spiral galaxies[339, 413, 414]. On the contrary, there is evidence that nearby dwarf star-forming galaxies (e.g. LITTLE THINGS dIrrs[411], the Large and Small Magellanic Clouds) show an opposite scenario, i.e the 'outside-in' mode[27, 415, 416]. Here, the star formation and subsequent mass assembly continue in the inner regions at later times. Therefore, our recent discovery of XUV disks in distant BCDs ($0.1 \leq z \leq 0.24$) raises the question if BCDs grow in a way unlike the general population of nearby dwarf star-forming galaxies[27] and motivates us to probe if all they follow the same suit till the present day. To do this, we take advantage of *AstroSat/UVIT's*[6, 7] commendable FUV imaging capabilities to understand the recent stellar mass assembly in local BCDs and look for the presence of XUV disks in these systems. The combination of *UVIT's* wide field of view and high spatial resolution with optical observations from ground-based telescopes will be advantageous to examine the stellar disks of nearby BCDs over a large region in the sky. We have recently obtained FUV observations, in part, for a sample of nearby BCDs with *AstroSat-UVIT* (P.I. Anshuman Borgohain, ID: A10-123).

5.2 Sample and Data

We build our sample of local BCDs based on a SQL (Structured Query Language) query to the Sloan Digital Sky Survey (SDSS) database server on its website[1]. We use the data release, 16 (DR16) which is the fourth data release of the fourth phase of the survey (SDSS-IV). Our sample is based on existing criteria presented in Almeida et al. 2008[92]. The criteria are primarily based on Gil de Paz et al. 2003[3] which are accordingly adjusted [92] to select BCDs using SDSS observations. However, there isn't a publicly available catalog of the BCDs identified in Almeida et al. 2008[92]. Therefore we use their criteria to perform a blind search for BCDs in the SDSS.

5.2.1 Sample selection

We use the following criteria from Almeida et al. 2008 [92] to select BCDs from the SDSS database.

- **Blue galaxies:** $\langle\mu_g\rangle - \langle\mu_r\rangle \leq 0.43$ mag arcsec^{-2}
  where $\langle\mu\rangle = 2.5\log(2\pi) + \mathrm{m} + 5\log \mathrm{R}_{50}$ is the average surface brightness, m is the apparent magnitude (foreground extinction corrected) and R_{50} is the radius containing 50% of the object's flux[417]. Since SDSS do not directly provide surface brightness values, so we use the above relation connecting apparent magnitude and size in our SQL query to define the surface brightness criteria.
- **Compact galaxies:** $\langle\mu_g\rangle < 21.83 - 0.47(\langle\mu_g\rangle - \langle\mu_r\rangle)$ mag arcsec^{-2}
- **Dwarf galaxies:** $\mathrm{M}_g >$ -19.12 + 1.72(M_g - M_r)
- $0.003 < z_{spec} \leq 0.3$

In our selection process, we avoid galaxies exhibiting AGN activity. For simplicity, we adhere to the basic photometric criteria outlined as above, and avoid imposing further constraints on the metallicity and SFR as was done in Almeida et al. 2008[92]. This could have resulted in a possible scenario where

[1] https://skyserver.sdss.org/dr16/

we would have had a single BCD candidate within a pointing. As this is a blind survey, we tried to optimise the sample size and the number of pointings to be requested for observations. Additionally, we avoid locations within ±30 degree of the galactic disk to minimise the foreground extinction and contamination. This yielded a total of 20,334 candidate BCDs. It is important to note here that these are potential BCDs and hence needs to be cross-checked. We propose observations with *AstroSat-UVIT*[6, 7] for those targets that would contain 2 or more BCDs. In order to target isolated BCDs, we use the same criteria used in Almeida et al. 2008[92]. A BCD is considered to be isolated if there are no sources brighter than ∼3 mag within $10R_{50}$ in the g-band. We also refer to their photo-z as per SDSS. The comparison of optical colours of local BCDs (G03) and the sample used in this research is shown in Figure 5.2.

5.2.2 Observations with AstroSat

For our *UVIT* FUV observations, we use the F154W broadband filter (λ_{mean} ∼ 1541 Å). The exposure times are motivated by the criteria to identify Type 1 XUV disks as defined in Thilker et al. 2007[18] (T07), i.e to detect young star-forming clumps in the outskirts of the galaxies. The *GALEX* UV imaging used by T07 had typical exposure times of ∼1500 sec which yielded 5σ FUV point source magnitude of 22.6 mag. In our previous work[358], which was based on ∼63 kilosec of *UVIT* FUV observations of the GOODS-South field, we were able to detect outer FUV clumps ranging from ∼25−27 mag with S/N≥3. So we want to go ∼3 mag or so deeper than *GALEX* and detect about ∼1 kpc sized structures with a S/N=3 in the outskirts of these candidate BCDs. The redshift of the BCDs selected is ∼0.03 or so. At this redshift, the angular scale is ∼0.6 kpc/arcsec. So we consider a circular aperture of diameter 1.5". In that, we estimate the exposure time required for a 26 mag FUV source to be detected with a S/N=3. The required exposure times are ∼20 kilosec or so. However, it is important to note that the total recovered exposure times in the final science-ready images may be smaller than expected. The loss of data may occur due to cosmic ray shower or inefficient L1/L2 conversion. The sky surface brightness for the above calculation is obtained from the *GALEX* tiles for the proposed pointings. We present the basic information on the *UVIT*

observations obtained so far in Table 5.1. From these observations, we have a sample of 25 BCDs.

UVIT source name	RA (degrees)	Dec (degrees)	GALEX sky (mag arcsec^{-2})	Recovered UVIT Exposure time (sec)
BCD_T1	209.5805	24.4970	28.9	7066
BCD_T2	129.6843	43.3722	29.0	10272
BCD_T3	168.9502	29.1882	29.1	5751
BCD_T6	172.5472	44.2552	29.0	14575
BCD_T7	182.6817	42.2642	29.2	19984
BCD_T8	197.7494	51.4872	28.9	16665
BCD_T9	216.0370	54.2522	28.6	24734

Table 5.1: **Information on the UVIT proposed observations, Proposal ID: A10-123** The tabulated exposure times are the ones from the reduced science-ready images.

5.2.3 Additional archival observations

All the BCDs have been detected using *GALEX*. We cross-checked the *GALEX* catalog of sources for each field and find that the FUV magnitudes of the BCDs using *GALEX* differ from what we measure using our *UVIT* observations by ∼0.1 mag. In addition to FUV observations with *UVIT*, we acquire good quality ground-based optical observations in the g (λ_{mean} ∼ 4730 Å), r (λ_{mean} ∼ 6420 Å) and z (λ_{mean} ∼ 9260 Å) bands from the DESI Legacy survey. It combines data from the DESI (Dark Energy Spectroscopic Instrument) Spectroscopic surveys, the Beijing-Arizona Sky Survey (BASS), the DECam (Dark Energy camera) Legacy Survey (DECaLS) and the Mayall z-band Legacy Survey (MzLS). We use the DR9 data release from the archive[2]. Basic information on the star formation and photometric properties of the selected sample is presented in Figure 5.1 and Table 5.2 respectively.

5.2.4 UVIT L1 data reduction

We obtain the level 1 (L1) data from the AstroSat archive[3] and use publicly available *UVIT* data reduction tool called CCDLab v3.0[421, 422] for generating science ready *UVIT* FUV images. The pipeline corrects for the fixed pattern noise (FPN), systematic bias in centroid positions and intrinsic dis-

[2]https://www.legacysurvey.org/
[3]https://astrobrowse.issdc.gov.in/astro_archive/archive/Home.jsp

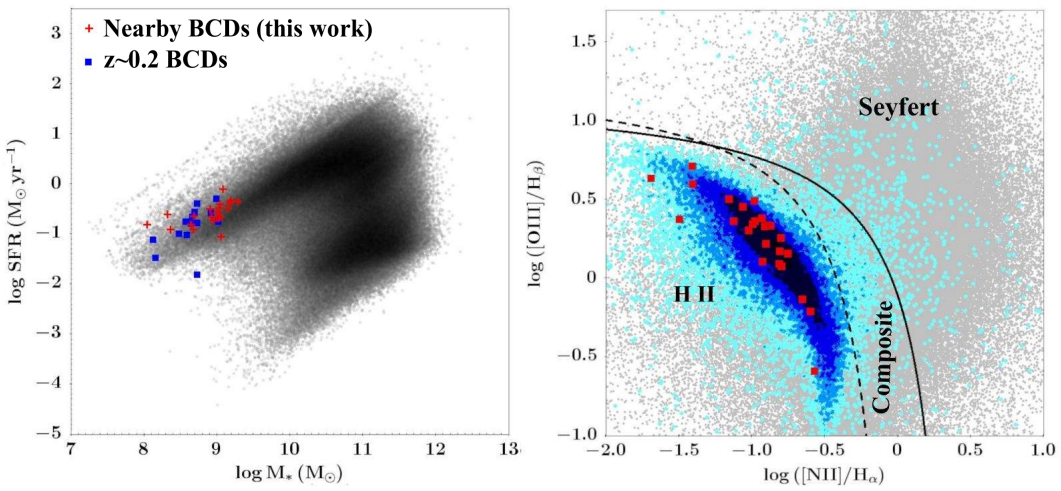

Figure 5.1: **Left:** SED-based integrated SFR and stellar mass of our sample BCDs. The estimates for the intermediate-z BCDs[358] are taken from the 3D-HST catalog[367]. The values for the nearby BCDs in this work and the background galaxies are taken from Salim et al. 2016[418] (we did not find values for 4 of our galaxies). **Right:** BPT diagram to show the emission from HII regions, composite spectrum type objects, and Seyfert galaxies. The red markers are the BCDs used in this work. The blue density markers represent those galaxies that satisfy the following criterion for being a dwarf galaxy: $M_g > -19.12 + 1.72(M_g - M_r)$; as mentioned above in the sample selection section. The solid and dashed curves used as described in Kewley et al. (2001)[419] and Kauffmann et al. (2003)[420]. The gray markers are the rest of the galaxies in SDSS.

tortions in the detector system. For more details, we refer the reader to the source articles[421, 422]. To avoid likely cosmic ray affected frames, we used a threshold of 4σ, where σ is the Poissonian noise of the median counts per frame overall observed frames. Each frame is then corrected for flat field bias that arises due to non-uniform detector sensitivity. The frames are then corrected for field drifts using the parallel visible observations in order to produce images per orbit. CCDLab also offers the flexibility to optimize the resultant PSF by correcting for any higher-order drift residuals. In the case of multi-orbit observations, each orbit image is aligned and coadded to produce the final image. The final science-ready image has a dimension of 4800x4800 pixels and a plate scale of 0.4167". We then use the GAIA catalog[423] with CCDLab to identify point sources and obtain the astrometric solution for the observations. Two proposed fields observed by *AstroSat* (ID: A10-123, P.I. Anshuman Borgohain) are shown in Figure 5.3.

BCD	z_{spec}	M_B	M_{FUV}	H_α flux	E_{B-V}	$SFR_{H\alpha}$	SFR_{FUV}
		mag	mag	x10^{-17} erg s^{-1}cm^{-2}	mag	$M_\odot yr^{-1}$	$M_\odot yr^{-1}$
LBCD01-1	0.0295	-17.67	-16.52	404.54 ± 4.49	0.09	0.0835 ± 0.0007	0.3275 ± 0.0076
LBCD01-2	0.0372	-17.73	-15.99	94.34 ± 2.02	0.08	0.0309 ± 0.0005	0.1984 ± 0.0087
LBCD01-3	0.0289	-17.31	-15.25	541.14 ± 5.86	0.2	0.1525 ± 0.0009	0.1487 ± 0.0059
LBCD01-4	0.029	-18.12	-16.53	766.39 ± 6.92	0.16	0.193 ± 0.0011	0.4246 ± 0.0095
LBCD01-5	0.0743	-18.95	-18.03	1397.32 ± 11.81	0.11	2.1186 ± 0.0126	1.4425 ± 0.0418
LBCD02-1	0.0345	-17.74	-16.21	244.65 ± 3.08	-0.02	0.0501 ± 0.0007	0.1852 ± 0.0050
LBCD02-2	0.0433	-17.74	-16.47	707.04 ± 5.32	0.13	0.371 ± 0.0018	0.3664 ± 0.0108
LBCD02-3	0.0262	-17.16	-15.34	114.36 ± 1.45	0.04	0.0158 ± 0.0002	0.0931 ± 0.0029
LBCD02-4	0.0393	-16.96	-15.59	316.97 ± 3.49	0.08	0.1158 ± 0.001	0.1371 ± 0.0056
LBCD03-1	0.0285	-17.74	-16.09	631.44 ± 6.24	0.15	0.1478 ± 0.0009	0.2713 ± 0.0081
LBCD03-2	0.0459	-18.28	-16.88	260.51 ± 3.63	0.22	0.1991 ± 0.0014	0.1999 ± 0.0123
LBCD03-3	0.0425	-17.99	-15.94	316.29 ± 7.71	0.06	0.1276 ± 0.0026	0.1776 ± 0.0086
LBCD03-5	0.0462	-18.31	-16.67	1239.29 ± 10.49	0.24	1.0356 ± 0.0042	0.6248 ± 0.0234
LBCD03-6	0.0288	-17.61	-15.86	208.77 ± 3.1	0.02	0.0331 ± 0.0005	0.1413 ± 0.0048
LBCD06-1	0.0246	-16.66	-14.73	218.2 ± 3.54	0.04	0.0271 ± 0.0004	0.0551 ± 0.0017
LBCD06-2	0.0246	-17.36	-15.50	456.47 ± 4.74	0.19	0.089 ± 0.0005	0.1801 ± 0.0046
LBCD06-3**	0.0272	-17.27	-16.59	- -	-0.17	- -	0.2631 ± 0.0024
LBCD06-4	0.0172	-16.83	-15.17	1004.91 ± 9.51	0.1	0.0726 ± 0.0005	0.1004 ± 0.0020
LBCD07-1	0.0228	-17.97	-16.80	575.67 ± 6.41	0.05	0.0626 ± 0.0006	0.3749 ± 0.0035
LBCD07-2	0.0227	-17.16	-15.69	168.18 ± 3.34	-0.1	0.0115 ± 0.0003	0.1147 ± 0.0026
LBCD08-1	0.0319	-17.14	-15.69	670.28 ± 6.11	0.02	0.1322 ± 0.0011	0.1229 ± 0.0023
LBCD08-3	0.033	-17.71	-15.72	367.04 ± 4.67	0.04	0.0822 ± 0.0009	0.1341 ± 0.0032
LBCD08-4	0.0295	-17.45	-16.36	401.74 ± 4.62	0.03	0.0692 ± 0.0007	0.233 ± 0.0036
LBCD09-1	0.0443	-18.12	-16.82	172.56 ± 3.12	0.01	0.064 ± 0.0011	0.3327 ± 0.0058
LBCD09-2	0.0338	-17.63	-15.89	300.03 ± 4.29	-0.01	0.061 ± 0.0009	0.1378 ± 0.0026

Table 5.2: **The sample of nearby BCDs** SFRs are both foreground and internal extinction corrected. ** For LBCD06-3, part of the spectrum that contains Hα is truncated. Here E_{B-V} is estimated using H_β and H_γ. Its OII flux derived SFR using the calibration of Kewley et al. 2004[424] is 0.0082 ± 0.0021 $M_\odot yr^{-1}$.

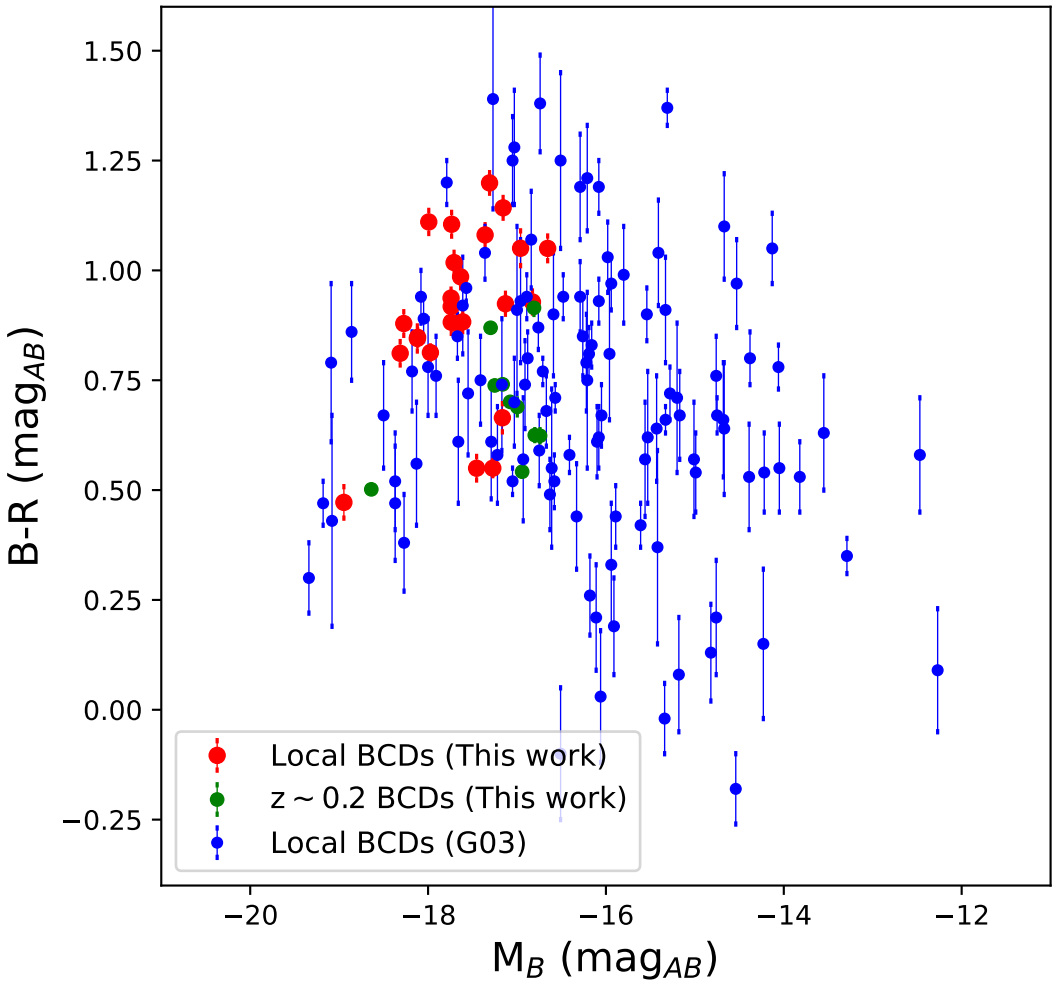

Figure 5.2: **Optical colours of BCDs.** Intermediate z BCDs from *GOODS-South* and nearby BCDs are over-plotted on the colour plot of local BCDs from Gil de Paz et al. (2003) [3].

5.3 Data Analysis

All measured magnitudes in the text are in the AB system and have been corrected for foreground i.e. Galactic extinction[361] and internal extinction unless specified. We use $\frac{A_\lambda}{E(B-V)} = 8.06$ for FUV passband[363].

5.3.1 Background subtraction and noise estimation

Proper background estimation is crucial to study the light distribution to very faint levels at galaxy outskirts. We use the same method for background estimation as described in Chapter 2. For all the selected BCDs, we obtain smaller cutouts of 100x100 arcsec and place boxes of 15x15 pixels size over each

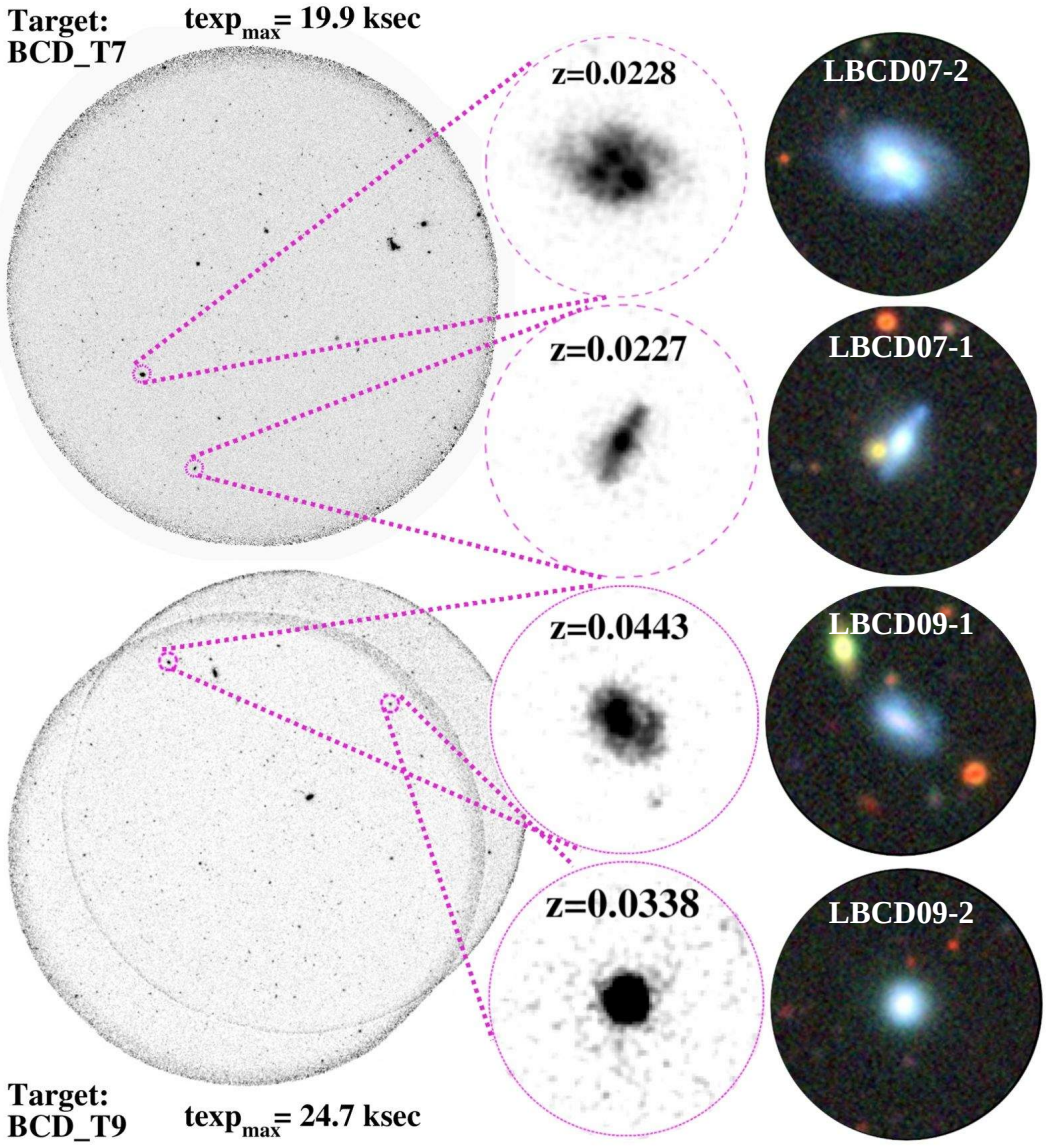

Figure 5.3: **AstroSat observation of two proposed fields.** The grey-scale images correspond to *UVIT* observations whereas the colour images correspond to DECaLS composite images. The circular zoomed-in images have radius of 20 arcsec each. AstroSat proposal ID: A10-123 P.I. Anshuman Borgohain

cutout avoiding the sources. Then we fit a gaussian to the obtained histogram of sky flux within the small boxes, which gives us the mean sky in each cutout. Similarly, we estimate the background rms by obtaining a distribution of rms values from each small box. In our shallowest and deepest FUV observations, the 5σ point source limits are $\sim$25.7 mag and $\sim$26.3 mag respectively within a circular aperture of diameter 1.5". These correspond to 5σ surface brightness limits ($\mu_{5\sigma,lim}$) of $\sim$26.2 mag arcsec^{-2} and $\sim$26.8 mag arcsec^{-2} respectively. The DECaLS images were already background subtracted and we estimate

the noise as described above.

5.3.2 PSF estimates

For each target field in the FUV, we select one representative and sufficiently isolated star by referring to the GAIA source catalog[423]. After cleaning any nearby contaminants we obtained their 1D profiles using IRAF[308] ELLIPSE task [307]. Before extracting their profiles, we also apply saturation correction [425, 426] to all the stars that have a total flux $\gtrsim$ 1 cps within a radius of 5". If the photon counts within a radius of 5" is greater than 3 cps, there is more than 5% saturation that affects the FWHM of the PSF. As in our previous works[357, 358, 427], we use a combination of a Moffat[356] for the core and an exponential profile for the outer wing.

$$I_{PSF}(r) = I_{c0}\left[1 + \left(\frac{r}{\alpha}\right)^2\right]^{-\beta} + I_{w0}\, e^{-r/R_s}, \tag{5.1}$$

where the first term represents the Moffat component and symbols have their standard meaning; R_s denotes the scale-length of the exponential profile, I_{w0} is the extrapolated central intensity of the wing component. The full-width at half-maximum (FWHM) is given as:

$$FWHM = 2\alpha\sqrt{2^{1/\beta} - 1}, \tag{5.2}$$

Here, we constrain the outer wing first by fitting it beyond 4" radius (second term in equation 5.1). Ideally, we would choose this radius to be 5", because the saturation effect beyond that point is assumed to be absent[426]. But not all stars are well extended and we need to have at least 3 datapoints in the PSF wing without arbitrarily large error bars. To preserve the homogeneity we start fitting the wing from 4" and beyond for all. Once we obtain the scale-length of the wing (R_s), we perform the complete fitting by keeping the R_s fixed. The FUV PSF FWHM values ranged from $\sim$ 1.1" - 1.7" with a median of $\sim$ 1.5". The best and the worst PSFs are shown in Figure 5.4 . For the DECaLS images, we directly used the PSF image provided in their archive. The median measured FWHM in the g, r and z bands are reported to be $\sim$

1.3", 1.2" and 1.1" respectively.

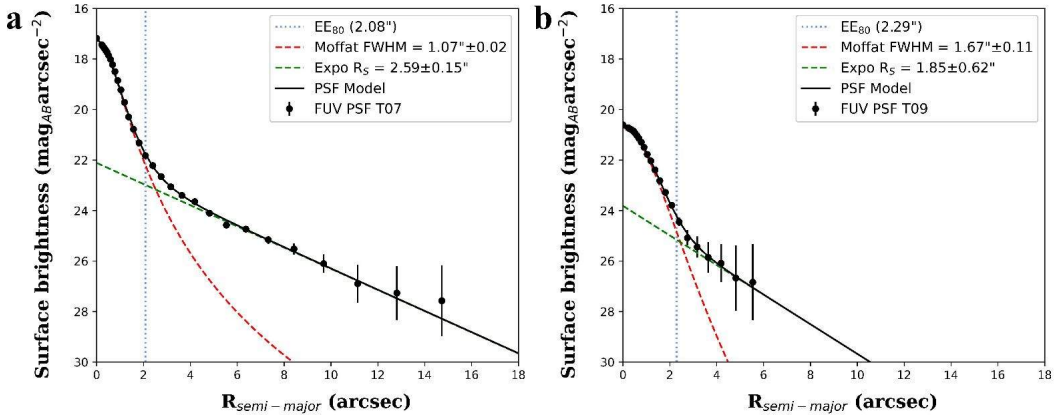

Figure 5.4: **Modelling of UVIT FUV PSF.** Figure shows the best (**a**) and worst (**b**) FUV PSF estimated for our proposed AstroSat observations of local BCDs. The error-bars represent 1σ errors.

5.3.3 2D GALFIT models

At first, we use the 2D fitting tool GALFIT[316, 317] to obtain a first-order structural analysis of the BCDs. Here we use single Sersic models to fit the images, which is one of the most widely used analytical galaxy models, in the F154W, DECaLS g, r, z bands. It is given as:

$$I(R) = I_{eff} exp\left(-b_n\left[(R/R_{eff})^{1/n} - 1\right]\right) \tag{5.3}$$

where I_{eff} is the surface brightness at effective radius R_{eff}. The effective radius (R_{eff}) encloses 50% of the light defined by the model. n is known as the Sersic index and b_n is a constant defined as b_n = 1.9992n - 0.3271, for 0.5 < n < 10 [428]. Otherwise b_n is such that $\Gamma(2n) = 2\gamma(2n,b_n)$. The modelling gives us the location, geometric parameters and total magnitude of the object in the image.

5.3.4 1D surface photometry

1D surface brightness profiles provide good insight into the overall structure of a galaxy. We use the PYTHON implementation of IRAF[308] ELLIPSE task[307] in *photutils* package to obtain 1D profiles of the BCD sample in the available wavelength bands. We make use of the geometric parameters (centre, effective radius i.e. R_{eff}, position angle, axis ratio) obtained from the

2D single Sersic modelling to set our initial guess parameters for 1D profile extraction. In each band, we fit one single isophote at $2R_{eff}$. Then, we fix the centre obtained from this elliptical isophote and using the rest of the GALFIT fit parameters as initial guesses, we rerun the isophote fitting in the range 0 $< R_{maj} < 6R_{eff}$, where R_{maj} is the semi-major axis length of the elliptical isophote. These 1D profiles then provide us with the sizes of the galaxies (R_{out}) in different wavelength bands. As described earlier in Chapter 2, this is the extent which the surface brightness profile reaches S/N = 3. As a standard of reference and historical reasons, we use the semi-major axis length at 25 mag arcsec^{-2} in the g-band as the 'R_{25}' radius. We will compare the obtained galaxy sizes and structural parameters with this in the later sections.

In this work, we are interested in investigating whether local BCDs also host XUV disks and understand their assembly and evolution. For this, we derive the structural parameters of the stellar disk across multiple bands. These galaxies are sufficiently larger than their respective PSF FWHMs and at the same time, they have similar PSFs across all the used bands. Since emission from the inner region is dominated by the central starburst and we are interested to understand the outer disk structure, we perform linear fitting to the profiles beyond the effective radii in the g-band ($R_{eff,g}$) and within the S/N =3 extents ($R_{out,\lambda}$). In the case of LBCD01-2 the FUV extent ($R_{out,FUV}$) is smaller than the $R_{eff,g}$. Upon inspection, it is seen that the galaxy is diffused in nature in the FUV. Hence we fit the disk within 1.5" and its $R_{out,FUV}$. The slope of the linear fits gives us the scale-length of the disk as $R_D = 2.5\log(e)/\text{slope})$.

In all cases, we correct for the cosmological dimming of the surface brightness by a factor of $(1+z)^4$ where z is the spectroscopic redshift of the object.

5.3.5 Integrated photometry

Galaxies do not have a well-defined extent or cut off at some radius. Throughout this thesis, we quantify the observable size as the one where the surface brightness reaches S/N = 3. But there may be faint emission beyond this extent which will be missed. In the past, masses of elliptical galaxies have been measured out to 5 times their effective radii[429]. Spiral galaxies are seen to

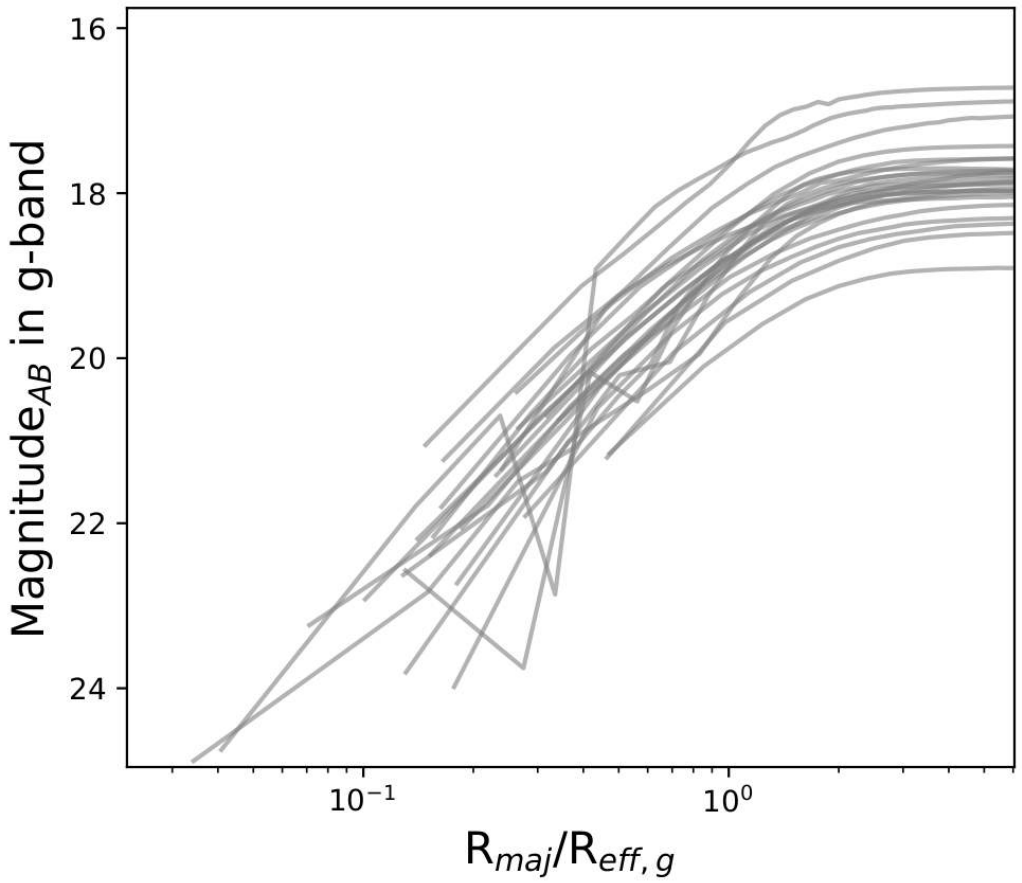

Figure 5.5: g-band flux growth curves of the BCD sample expressed in AB magnitudes. The x-axis is the ratio of the semi-major axis length to the effective radii of the respective BCDs.

extend out to 4-5 scale-lengths. In our case, most of the galaxies extended out to 2-4 times their effective radii (R_{eff}) in their respective passbands. Upon further inspection of the cumulative flux growth curves (Figure 5.5) obtained from isophotal ellipse fitting in the previous section, we find that the g-band profiles begin to flatten out beyond 4-5R_{eff}. Therefore, we use a fiducial value of 4R_{eff} as the aperture to measure fluxes of the galaxies. The aperture geometry at 4R_{eff} is taken from the table of fitted ellipses obtained from 1D surface photometry which is described in 5.3.4.

5.3.6 Star-formation rates

We present the star-formation rates in the BCDs (recent and instantaneous) in Table 5.2 which are obtained as under: We convert the measured FUV fluxes into SFRs[30] that traces recent star formation within the past ∼100 Myr. It

is given as follows:

$$SFR\ (M_{\odot}\ yr^{-1}) = 1.4\ \times\ 10^{-28}\ L_{\nu}\ (ergs\ s^{-1}\ Hz^{-1}) \tag{5.4}$$

We estimate the star-formation rates (SFR) of the galaxies using SDSS H_{α} fluxes and calibration of Kennicutt[30]. It traces the instantaneous star formation within ∼10 Myr and given as follows:

$$SFR(H_{\alpha}) = 7.9 \times 10^{-42} \times L_{H\alpha}(ergs\ s^{-1}) \tag{5.5}$$

The SDSS spectra do not reflect the total H_{α} emission in these galaxies because it only samples the central 3" diameter of the galaxy and hence it. In both cases we correct for the effects of foreground, i.e. Galactic extinction and internal reddening of the target due to dust as per the Balmer decrement method and using a Calzetti extinction curve[393] given as

$$f_{corr} = f_{obs} \times 10^{0.4\ k(\lambda)\ E(B-V)} \tag{5.6}$$

$$E(B-V) = 1.97 \times \log\left[\frac{(H_{\alpha}/H_{\beta})}{2.86}\right] \tag{5.7}$$

5.3.7 Stellar mass estimates

We estimate the stellar masses of the BCDs in two ways. Firstly, we use the stellar mass-to-light (M/L) calibration for g-r colour and the r-band fluxes [430]. It is given by

$$log_{10}(M/L) = a_r + (b_r \times (g-r)) \tag{5.8}$$

where M/L is in solar units and $a_r = 0.306$, $b_r = 1.097$. Secondly, we use the FUV SFRs and assume a constant SFH for 100 Myr to obtain the young stellar masses. We correct the g-r colour, r-band and FUV luminosity for foreground and as well as internal extinction (described above in section 5.3.6).

5.3.8 Radial gradients

Due to the proximity of the sample and similar multi-wavelength imaging quality of the sample, we can obtain spatially resolved properties to some extent. This will allow us to assess their assembly and evolutionary status. One thing that should be kept in mind when dealing with colour gradients is to ensure that we are sampling the same physical area of the galaxies across different wavelength bands. For this, we use the g-band fitted elliptical isophotes to extract surface brightness profiles of the galaxies across all the other bands.

5.3.8.1 FUV-r colour gradient

Colour indices reflect a number of galaxy properties such as metallicity, star formation rate, stellar age, dust content etc. The assembly and evolutionary history of a galaxy over its lifetime is reflected in the spatial variation of the above properties. Many studies in the past have analysed radial colour gradients that correlate with various galaxy properties[431–435] and provide insight into their physical origin. However, choosing the right colour is of paramount importance in order to infer galaxy properties. For example, there is the age-metallicity degeneracy[436] observed in the case of optical colours which cannot be corrected without prior information. UV-optical colour is however insensitive to this degeneracy problem when ages are less than 1 Gyr and important in the case of recent and low level star formation[433, 437, 438]. Here we make use of the FUV-r colour index as a tracer of the young stellar population. A value less than 5, as used in Lemonias et al. 2011 indicates young stars [2]. The value 5 comes from literature where blue star-forming galaxies are observed to reach up to this point[439] and this corresponds to a D_n4000 break index of 1.7 [440]. This in turn indicates a stellar population less than 1.5 Gyr formed in an instantaneous burst of star formation[441].

We estimate the mean logarithmic gradient ∇(FUV-r), of the galaxies by performing a linear least squares fit within 1.5" (which is the largest median FWHM among all bands) and $2R_{eff,r}$ (R_{eff} in the r band) to the FUV-r colour profile[435]. This is similar to measuring $(\text{FUV-r})_{R=1.5''}$ - $(\text{FUV-r})_{2R_{eff}}$. The

gradient is given by

$$\nabla(FUV - r) \equiv d(FUV - r)/d\log r \tag{5.9}$$

5.3.8.2 Stellar mass density profiles

We obtain the stellar mass density profiles of the galaxies using the g and r band colour profiles and the calibration of Bell & de Jong [430] as mentioned above in section 5.3.7. Also, the young stellar mass density profiles are obtained by converting the FUV surface brightness profiles into star formation rate surface density (SFRD) profiles and multiplying them by 100 Myr. We correct for the foreground extinction as well as internal extinction for the stellar mass profile estimates.

5.3.8.3 sSFR profiles

Radial sSFRs, i.e. the radial variation of the SFR per unit mass of the galaxy, serve as another diagnostic to understand where active star formation and mass assembly is taking place. To obtain this, we use the FUV star-formation rate profiles and stellar mass profiles obtained above.

5.3.9 Probing the LSB region

Our analysis reveals that the observed FUV sizes of the galaxies are either the same or smaller than the optical extents. We find from our analysis above that the azimuthally averaged 1D FUV surface brightness profiles reach only around $\sim$26 mag arcsec^{-2} with S/N$\geq$3. The expected surface brightness levels may not be reached as faint and unresolved sources will contribute to the background and noise. We require our 1D FUV surface brightness (μ_{FUV}) profiles to reach at least 27.25 mag arcsec^{-2} or beyond with S/N$\geq$3 to inspect for Type 1 or Type 2 XUV disks as per T07. Hence, the depth of the FUV observations is not sufficient to probe into the Type 1 or Type 2 XUV nature of the BCDs. We follow indirect measures to look for indications in/not in favour of XUV emission. This is firstly motivated by one of the methods in T07 to identify Type 2 XUV disks and described as follows. We define a low surface brightness (LSB) region which is analogous to the LSB region defined

in T07 for a Type 2 XUV disk. In T07, this is a region within a contour that encloses 80% of the K band flux and a contour at 27.25 mag arcsec^{-2} in the FUV. For our case here, we define our LSB region as the one within R_{80} (that encloses 80% of r band flux and should be comparable to that in the K-band) and $R_{27.25}$. We define our $R_{27.25}$ as the distance at which the fitted outer FUV disk is expected to reach μ_{FUV}=27.25 mag arcsec^{-2}. We inspect the FUV-r colour in this LSB region and term this colour as FUV-r_{LSB}.

We then measure $\Delta L_{x,FUV}$ which is the fraction of FUV flux in the LSB region defined above. This term is analogous to the FUV light fraction that we measured in the XUV regions of z ∼0.2 BCDs presented in Chapter 2. However, there is a difference that in Chapter 2 we integrated the intrinsic profiles of the BCDs to avoid the PSF blurring effect in the FUV. In the present case, due to similar spatial resolution, the blurring across all bands is similar and therefore we measure the light fraction directly from the observed images. Additionally, the area where we integrated the light (in Chapter 2) was enclosed within the S/N=3 optical and FUV extents. In this chapter, we had to modify these boundaries because we cannot define a region similar to the XUV region defined for distant BCDs. In the case of distant BCDs, the FUV extents, based on S/N, were larger than the optical that implicitly defined an XUV region. Whereas the S/N = 3 spatial extent of the local BCDs in the FUV is either the same or smaller than the optical extent. We also measure $\Delta L_{x,r}$ (value in the r band) for comparison. These measurements are motivated by a previous study by Lemonias et al. 2011[2] (hereafter L11). We use these measurements in the LSB region to probe the existence of XUV disks in these BCDs and discuss them in the following section.

5.4 Results and Discussion

5.4.1 Morphology and sizes

Our 2D GALFIT models, using single a Sersic function, reveal that the effective radii or the half-light radii (R_{eff}) of the local BCDs are similar across FUV to optical wavelengths; with 5 of them having smaller half-light radii in the

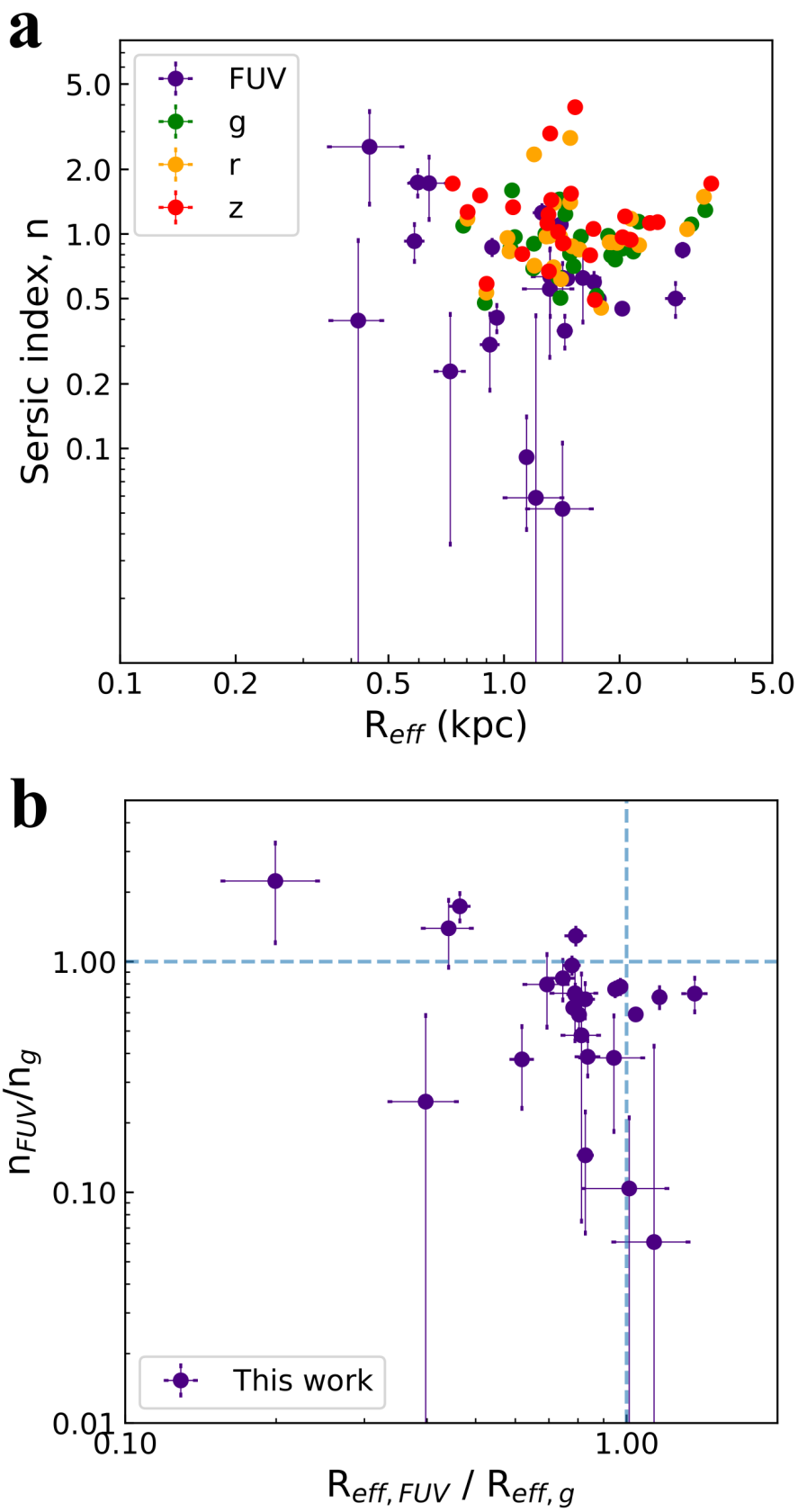

Figure 5.6: **Results from 2D GALFIT modelling. a**: Figure shows the estimated Sersic indices n and effective radii (R_{eff}) in the FUV, g, r and z bands. **b**: The comparison of FUV and g-band Sersic parameters.

FUV. About a third of the BCDs have smaller FUV Sersic indices (n) than the optical indicating cored profiles as opposed to the disky nature in optical bands (Figure 5.6). We do not see vast differences in the R_{eff} and Sersic indices (n) among the optical bands. A previous study (Vulcani et al. 2014) shows that the R_{eff} of galaxies are seen to be correlated with wavelength - with smaller values at longer wavelength. However, this relation is also dependent on the Sersic index and colour of the galaxies[442]. In our case here, we fail to find such a correlation. But going into it in detail is beyond the motive of this work. Also, the obtained 2D models here are first-order estimates of the overall galaxy structure. The galaxies may contain multiple components which will be explored further in a future work.

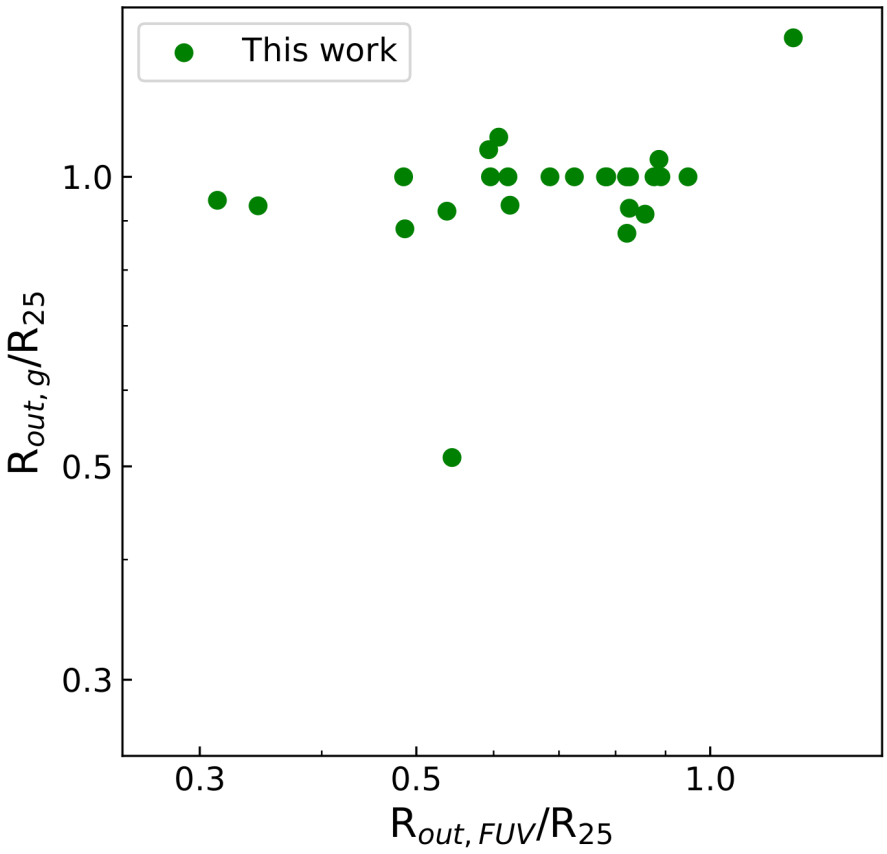

Figure 5.7: **FUV and optical sizes of the BCDs.** Figure shows that the S/N = 3 based FUV extents of the BCDs are similar or smaller than the optical counterparts.

Our 1D multi-wavelength surface photometry of the BCDs, based on S/N=3, reveals that the FUV spatial extents ($R_{out,FUV}$) are smaller than or similar to those in the optical wavelengths ($R_{out,opt}$, Figure 5.7). Based on these observa-

tions we find that the local BCDs in our sample are not spatially extended in the FUV. Our FUV observations have a median $\sigma = 3.4 \times 10^{-5}$ counts/s/pix which corresponds to a 5σ point source magnitude limit, $mag_{lim,median} = 26$ mag (that translates to 26.5 mag arcsec^{-2}) in a circular aperture of diameter ∼1.5". As mentioned above, the observed FUV surface brightness profiles also reach close to this level. We point out here that the exposure times of the reduced science-ready images are of the order of a few 10^3 to $\sim 10^4$ seconds and hence the observations are shallow as compared to what we had in the case of *GOODS-South*. Therefore there is always a possibility that we may trace even fainter levels in the FUV with deeper observations. A complete list of figures displaying the S/N=3 extents are displayed in the Appendix of this Chapter in Figures 5.19 - 5.24.

5.4.2 Disk mass assembly

We assess the disk assembly of the BCDs multifold. Firstly, we compare the multi-wavelength outer disk scale-lengths and find that they are similar for most cases. As presented in the histogram in Figure 5.8, the scale-lengths (R_D) ranged from ∼0.5 - 3 kpc. We assess the disk scale-length variation across all the bands for better insight. We find that for 7 (8) of the BCDs, the FUV scale-lengths of the BCDs are larger than both in the g and r (g and z) bands. As we have observed in the case of distant BCDs in our previous work (Borgohain et al. 2022[358], hereafter B22), such larger FUV scale-lengths imply a larger fraction of young stellar population at larger radii which is indicative of recent outer disk assembly. A complete list of figures displaying the 1D surface brightness profiles is presented in an Appendix of this Chapter in Figures 5.19-5.24.

As described above, ∇(FUV-r) represents the overall colour gradient of the galaxies. Previous studies have shown flat colour gradients in low-mass galaxies[435] and reveal that most of them have similar aged population at all radii and that they are assembling their disks in a self-similar manner. However, there are other studies that also indicate an 'outside-in' scenario where recent mass assembly is evident in the inner parts[27, 413, 433] and that only massive galaxies grow from the inside-out. The environment of the

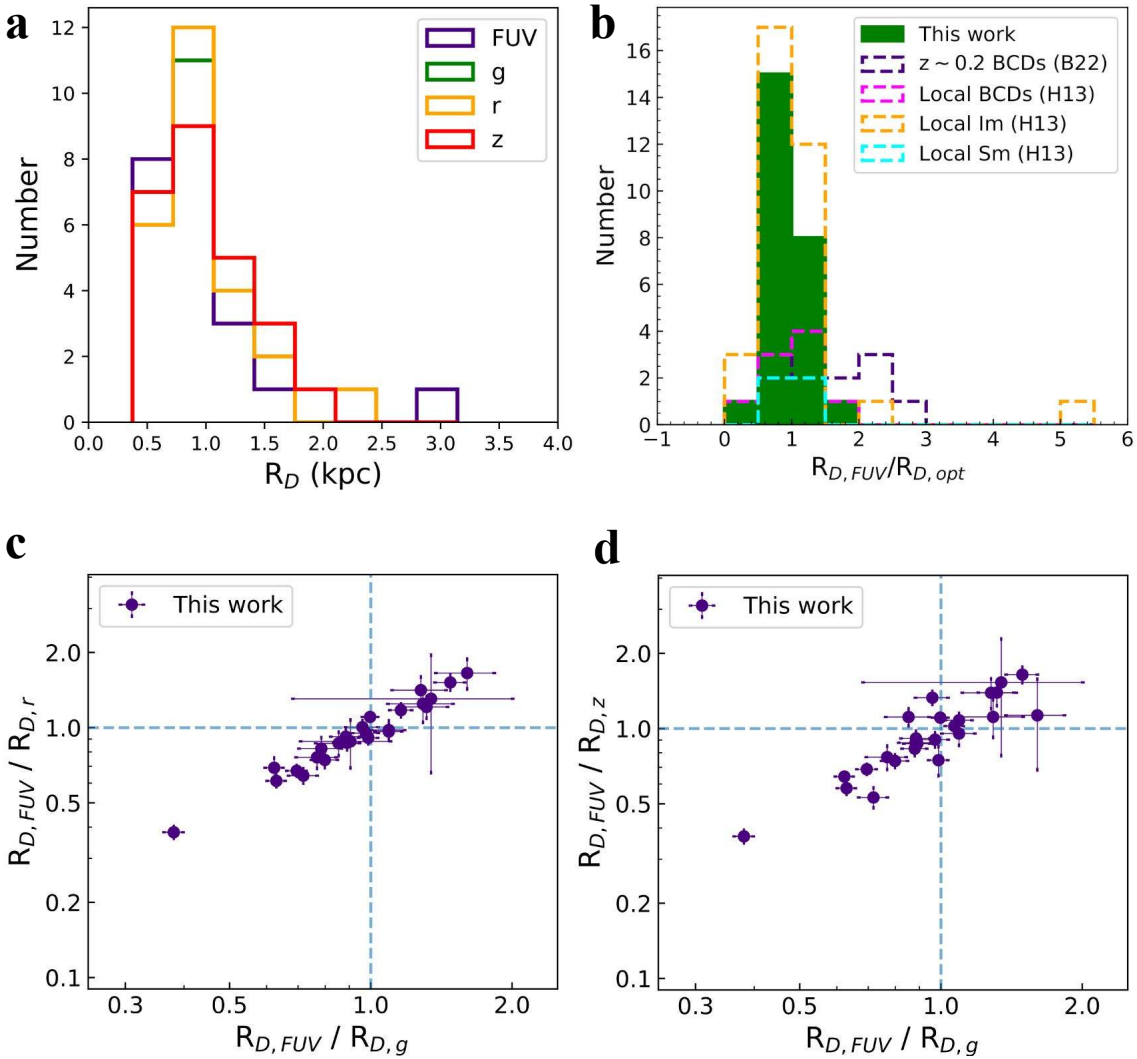

Figure 5.8: **Results from 1D outer disk modelling. a**: It shows the distribution of estimated outer disk scale-lengths in the specified broadband filters. **b**: It shows the FUV-to-optical (g-band) scale-length ratios and their comparison to previous work on z∼0.2 BCDs [358] and other local dwarf galaxies [334]. The FUV scale-lengths of distant BCDs are larger than the local ones studied here. **c, d**: Comparison of FUV scale-lengths to scale-lengths in all optical bands. It shows that 7 BCDs in this work have FUV scale-lengths larger than all the optical bands used in this study. All error-bars represent 1σ errors.

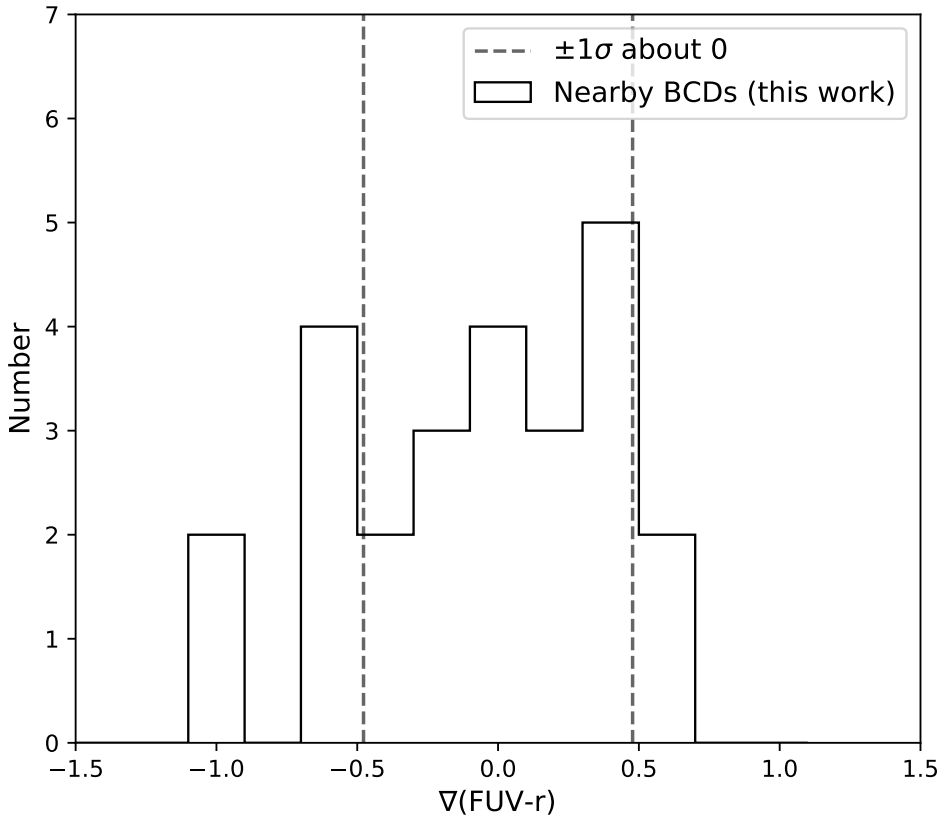

Figure 5.9: **FUV-r colour gradient of local BCDs.** This shows the distribution of the FUV-r colour gradient of obtained for the BCD sample by fitting a linear relation to the FUV-r profile. The vertical dashed lines mark the $\pm 1\sigma$ scatter about FUV-r = 0 which is $\sim$0.48.

galaxies is also important to take into consideration as massive neighbours or crowded fields tend to affect the observed outcome. Nevertheless, we keep our discussion here to isolated BCDs. In Figure 5.9, we show the distribution of estimated gradients for our BCDs. It reveals that 8 BCDs fall outside the 1σ scatter of the distribution (6 of them on the negative side). Negative gradients imply blue FUV-r colours in outer regions which is also indicative of an ongoing assembly of the outer parts of these BCDs.

We try to look for trends in the obtained colour gradient (∇(FUV-r)), the specific star-formation rate (sSFR), the stellar mass and the optical g-band size at 25 mag arcsec^{-2} (R_{25}) of the BCDs. We do not find any visible trend among the mentioned physical parameters. This is presented in Figures 5.10 and 5.11.

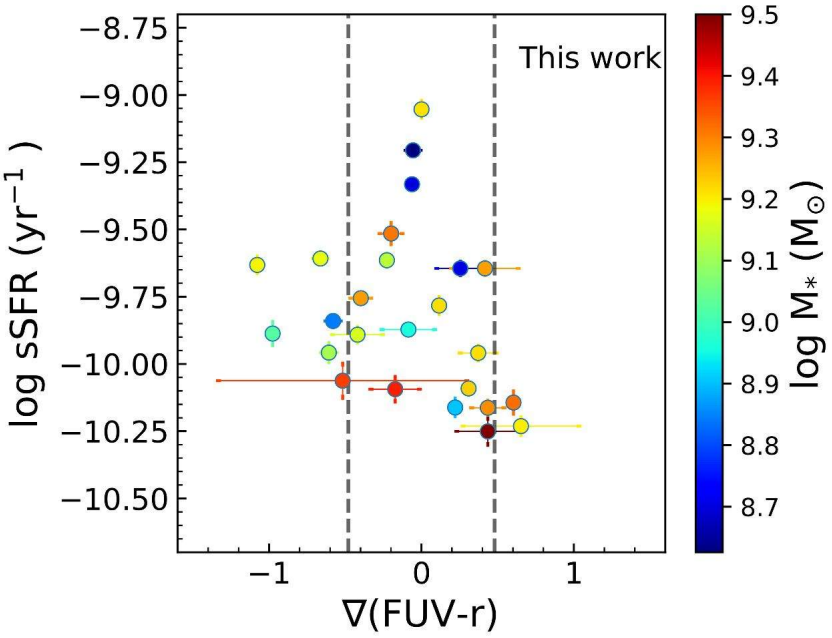

Figure 5.10: **sSFRs, colour gradients and stellar masses of local BCDs.** Figure shows the estimated sSFR versus the colour gradients. The vertical lines represent the 1σ scatter as shown in Figure 5.9. The colour bar axis on the right shows the stellar masses of the BCDs. Error-bars are 1σ.

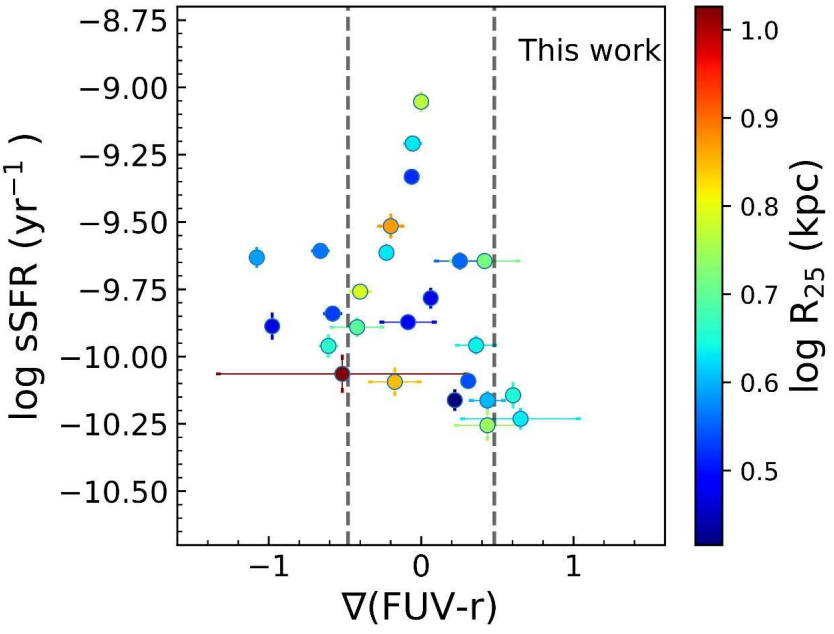

Figure 5.11: **sSFRs, colour gradients and R_{25} sizes.** Same as Figure 5.10 but the colourbar axis represents the radius where the g-band surface brightness is 25 mag arcsec^{-2}. Error-bars are 1σ.

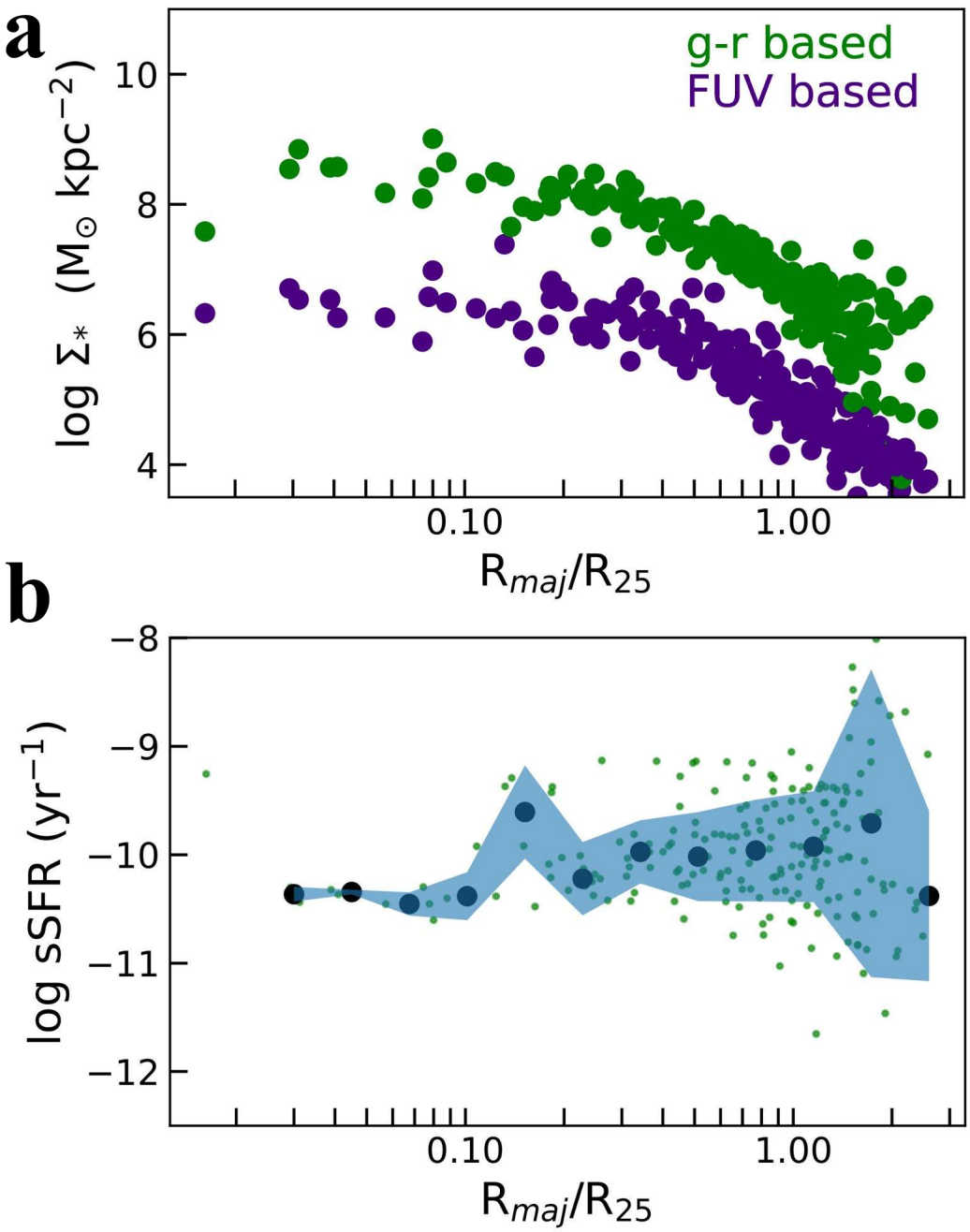

Figure 5.12: **Stellar mass density and specific star formation rate profiles. a**: Figure shows the stellar mass surface density based on g-r colour (green) and the young stellar mass (indigo). **b**: Figure shows the combined sSFR profiles of all the BCDs. The black markers represent the median sSFR in a given annulus and the blue filled region bound the $\pm 1\sigma$ scatter about the median sSFR profile.

Figure 5.12 shows the radial stellar mass density (total and young) and the sSFR profiles of the BCDs. The stellar mass density profiles are seen to vary together similarly with distance. The average sSFR profile appears to be flat indicating that the assembly of local BCDs occurs in a self-similar manner in general throughout the disk. However, there will be individual

cases with an increasing outer sSFR. Such cases indicate an increased recent assembly in the outer parts. Nevertheless, we need a bigger sample of low-mass galaxies to present a more robust explanation for this. As shown in Figure 5.1, photometrically selected dwarf galaxies also exist in the region defined for Seyfert and composite spectrum type of galaxies. In fact, previous studies on intermediate-z (0.1 - 0.3) low-mass galaxies have shown that 10-30% of them host low-luminosity AGNs[443]. We plan to study a larger sample of low-mass galaxies in the future to understand the role of both star formation and AGN activity on their assembly and growth.

5.4.3 Assessing the XUV nature of nearby BCDs

As shown in Figure 5.13, we find that the fraction of FUV light in the LSB region as described above in section 5.3.9 is larger than the r-band flux for 7 BCDs (ignoring the outlier). In the adjacent figure, the FUV-r colour also becomes bluer indicating a younger population of stars. We should note here that having blue outer regions is not a sufficient condition for having XUV disks. It may indicate that star formation in the inner regions has quenched - e.g. due to bulge formation. So we mark the BCDs with red which have FUV scale-lengths greater than those in the g,r and z bands. Of these, 4 BCDs also have outer FUV light fraction greater than in the r-band.

We compare the FUV light fraction ($\Delta L_{x,FUV}$) in the LSB (/XUV) region (described in section 5.3.9) versus the FUV-to-optical scale-length ratios ($R_{D,FUV}/R_{D,opt}$; opt refers to g-band in this work) of these local BCDs to that of the distant counterparts in B22 (Figure 5.14). Please recall that the LSB and XUV region refers to different parts of the galactic disk. The LSB region for these local BCDs is defined as the area within an elliptical isophote that encloses 80% of r-band flux and an isophote where the extrapolated FUV outer disk profile is expected to reach $\mu_{FUV} = 27.25$ mag arcsec^{-2}. Whereas, the XUV region for distant BCDs (defined in Chapter 2) is the area within the S/N=3 optical and FUV extents. So a direct one-to-one comparison will not be accurate here. But it should give us some indication of the possibility of XUV disks in the nearby BCDs. We find that 7 of the nearby BCDs have $\Delta L_{x,FUV} > 0$ and FUV scale-lengths ($R_{D,FUV}$) greater than the g-band optical

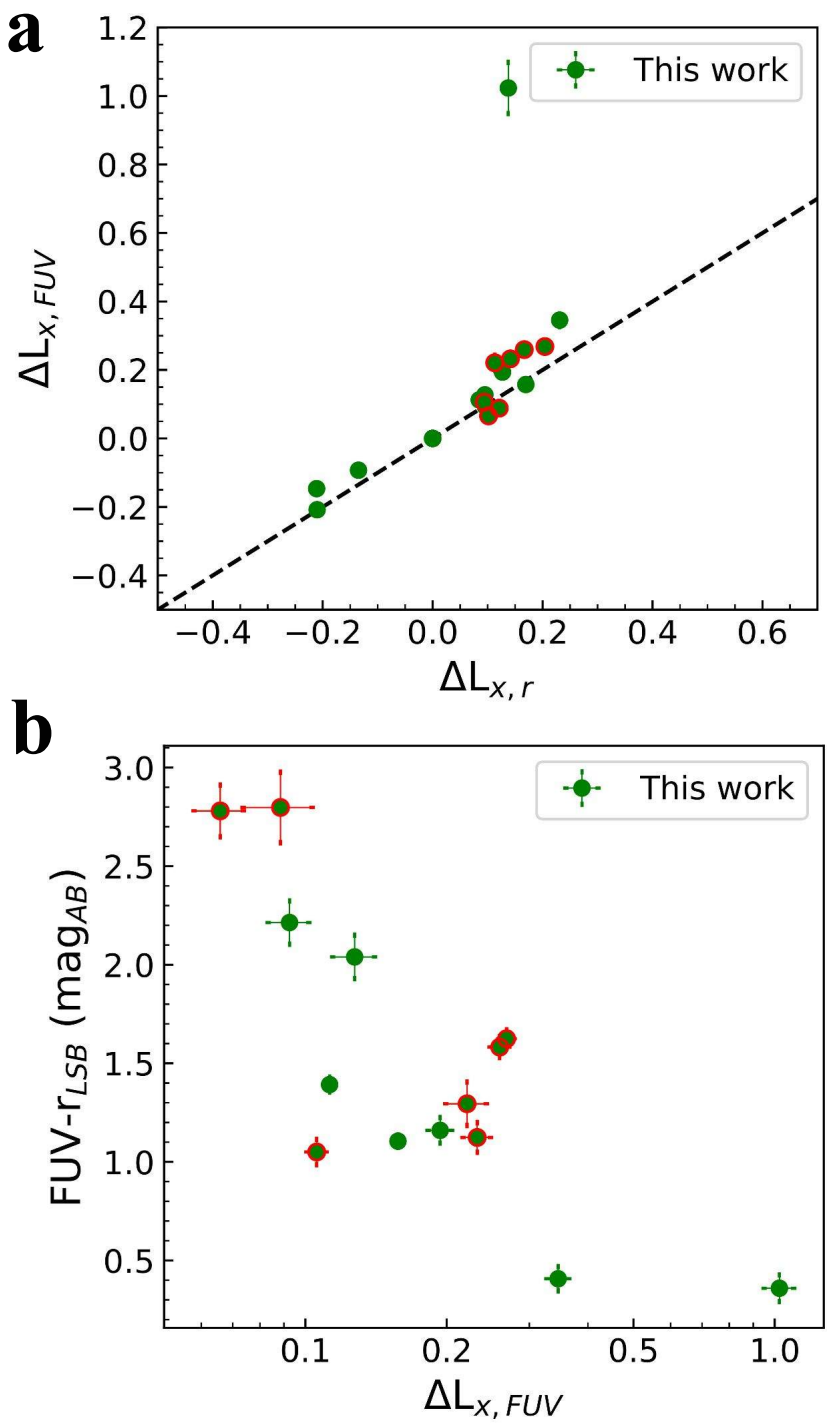

Figure 5.13: **Outer FUV and r-band light fractions and colours. a**: This shows the FUV light fraction versus the r-band light fraction in the outer LSB region. **b**: It shows the outer LSB FUV-r colour versus the outer FUV light fraction. In both cases, red markers are for those BCDs that have larger outer FUV disk scale-lengths ($R_{D,FUV}$) as compared to the optical counterparts which is demostrated in Figure 5.8. Error-bars are 1σ.

($R_{D,opt}$). Based on our observation in the case of B22 BCDs that host XUV disks, these 7 BCDs may be considered candidates that host XUV disks. Incidentally, 4 of them also have blue FUV-r colour in the LSB region as compared

to the overall galaxy colour and the FUV light fraction greater than the r-band light fraction in the LSB region ($\Delta L_{x,FUV} > \Delta L_{x,r}$). These are identified later in Table 5.3.

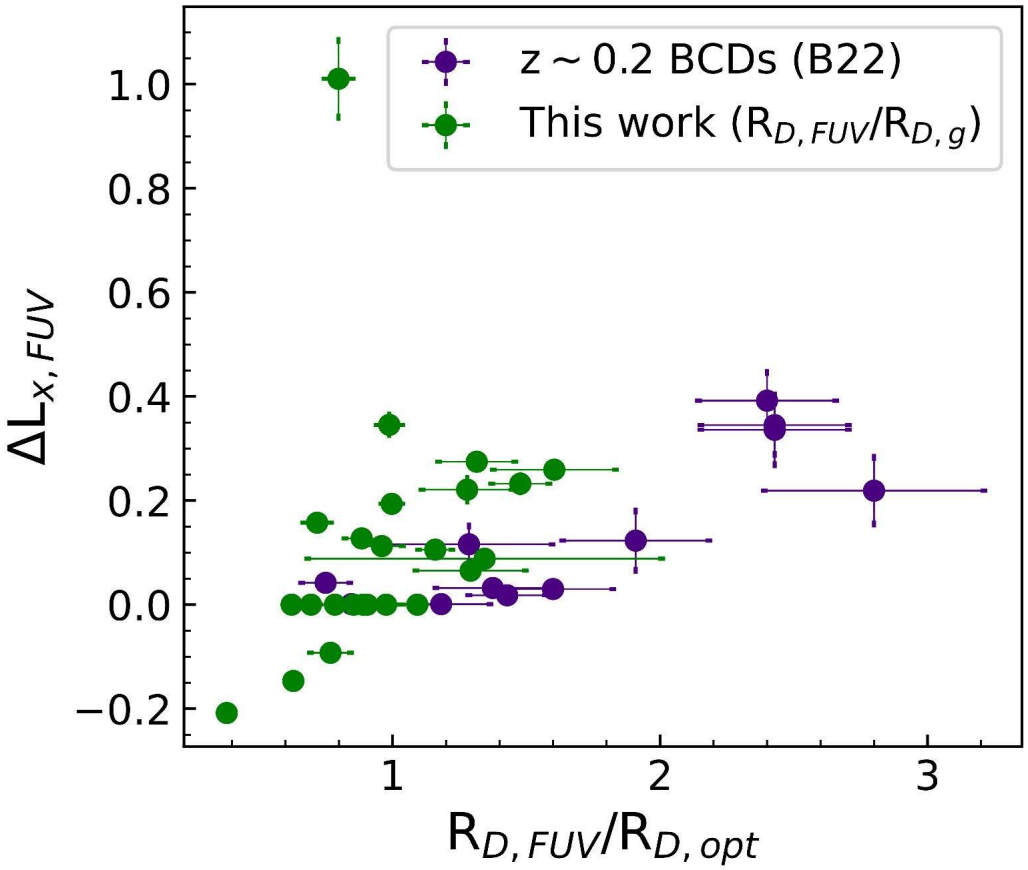

Figure 5.14: **Relation between excess UV light and disk scale-length of local BCDs.** Figure shows a comparison of the outer FUV light fraction and the outer FUV-to-optical scale-length ratios with distant BCDs studied in B22. Error bars are 1σ.

In Figure 5.15, we try to compare our results with that of L11. Here, we compare our results two-fold because our definition of the LSB region in our case and the XUV region in L11 is different. Firstly, we see that for the BCDs for which we can obtain an LSB colour, the outer colour becomes bluer monotonically with the galaxy colour. We mark with red (boundaries of green markers) if the FUV scale-lengths are larger than the optical ones. We see that there are 7 such cases. However, out of these 7 BCDs, we find 4 of them to have a bluer outer LSB colour as compared to the overall galaxy. This is an indication that the outer region has younger stars (FUV-r<5). In L11, the XUV region is the area bound by the FUV surface brightness contour at 27.25

mag arcsec^{-2} and 29 mag arcsec^{-2}. The observed profiles do not reach such surface brightness levels. So we extrapolate the fitted outer disk FUV and r-band profiles to obtain modelled FUV-r$_{LSB}$ colour for our BCDs within the region defined by the above two surface brightness levels. These values are marked as green stars. We find that for 6 BCDs, including the same 4 BCDs as mentioned above, the outer colour is bluer than the overall galaxy.

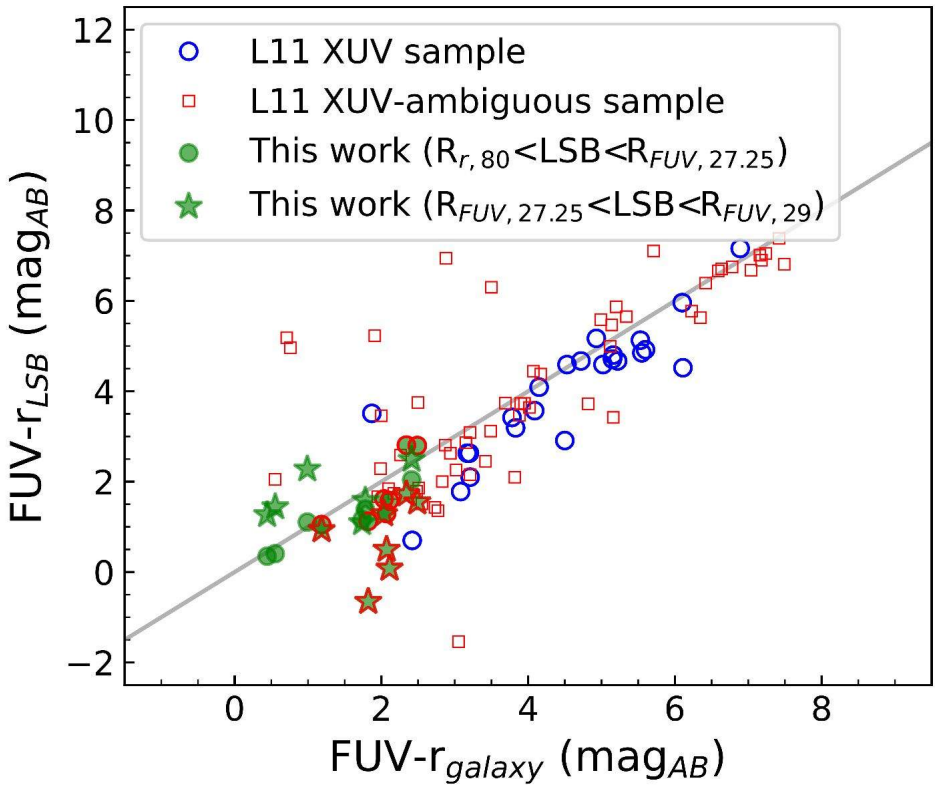

Figure 5.15: **Comparison of outer FUV-r colour to full galaxy.** This figure shows the FUV-r colour in the outer LSB region versus the FUV-r colour for the full galaxy. The full galaxy colour is measured within an aperture of R_{25} radius. We compare the results obtained from our definition of an LSB region (green filled circles) and from L11 definition of XUV region (green filled stars). The blue circles denote the XUV disks identified in L11 whereas the red squares represent those for whom the XUV nature could not be ascertained in L11. Grey line represents same outer and overall galaxy colour.

To summarize, we find the following: a) 4 BCDs with larger FUV scale-lengths have outer FUV fraction larger than in the r-band and blue LSB colors compared to the whole galaxy (Figure 5.13). b) 7 BCDs have FUV fraction > 0 and FUV scale-lengths greater than optical at the same time (Figure 5.14). c) 4 BCDs have FUV scale-lengths greater than optical and bluer outer colours as compared to the overall galaxy at the same time. If we consider the L11

definition of an XUV region, we have 6 such cases (Figure 5.15). Thus we can safely claim an XUV disk for 4 BCDs in the sample which satisfies all the criteria used to assess the XUV nature. These can be identified in Table 5.3.

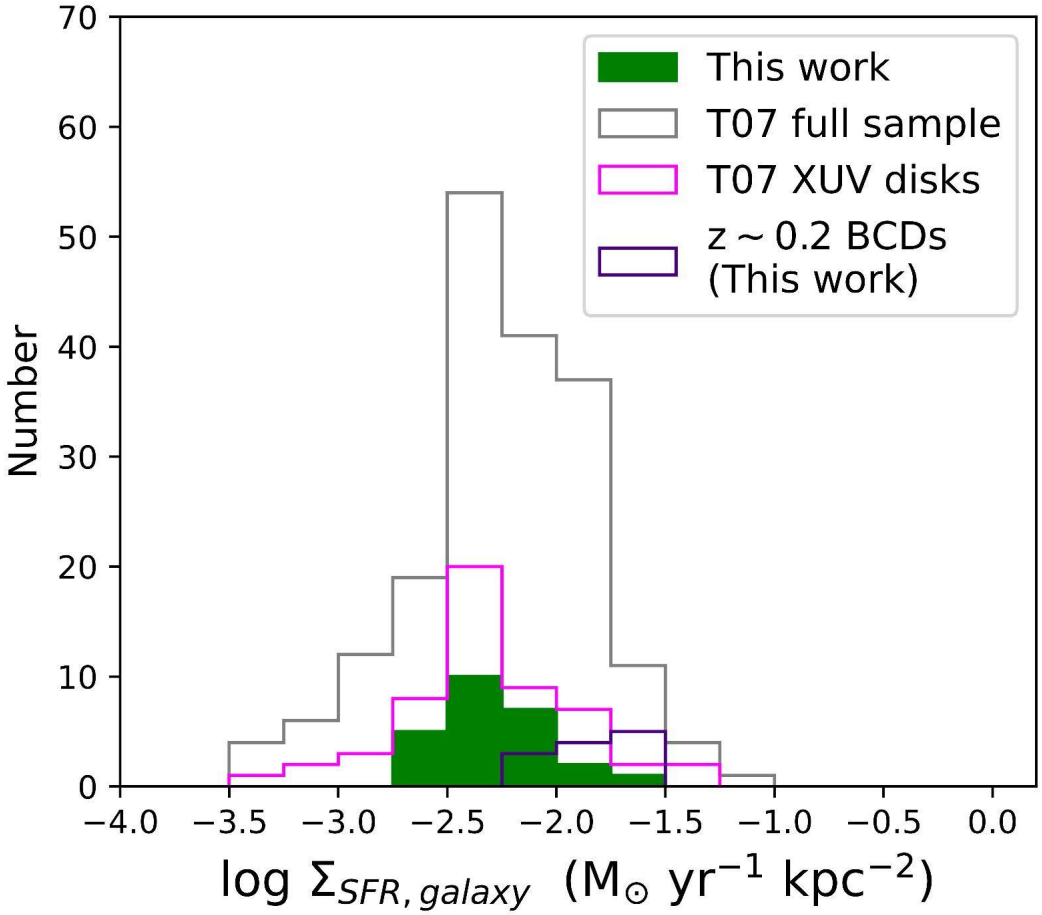

Figure 5.16: **Comparison of global SFRD in local BCDs and local XUV disk galaxies.** Figure shows the SFRDs of local BCDs and T07 XUV disks. In all cases, the SFR estimates are normalized within an area of R_{25}.

Figure 5.16 shows a comparison of the star formation rate surface density (SFRD) of our sample of local and z∼0.2 BCDs with XUV disk sample of T07. The SFRDs in BCDs and local XUV disks do not show any unique difference and the global star formation going on in the local BCDs (whether they do or do not possess an XUV disk) is similar to other local star-forming galaxies. The distant BCDs (B22) however have higher SFRDs on an average than the local BCDs being considered here.

Figure 5.17 shows the FUV-r colour of the outer disks of BCDs. The plot also shows a subset of the L11 sample which contains confirmed as well as ambiguous XUV disks. It indicates that apparently there isn't a dependence

of the presence/absence of XUV disks on the stellar mass of local BCDs and other local galaxies. Whether an XUV disk exists or not, the outer disk colours become bluer with decreasing stellar mass. This indicates that the origin of XUV disks is more likely to have an external origin such as gas accretion. Such a scenario of galaxy stellar mass growth via gas accretion is in line with the predictions of the ΛCDM framework. However, our study is not without caveats. We do not have information on the dust, metallicity or gas distribution in the outer regions of these galaxies which is one of the main caveats of the analysis. Since star-forming dwarf galaxies show flat metallicity gradients in general, we assume that the chemistry in the outer regions resembles that in the inner regions for our BCDs. Galaxy-wide spectra and HI distribution will be able to shed further light on this.

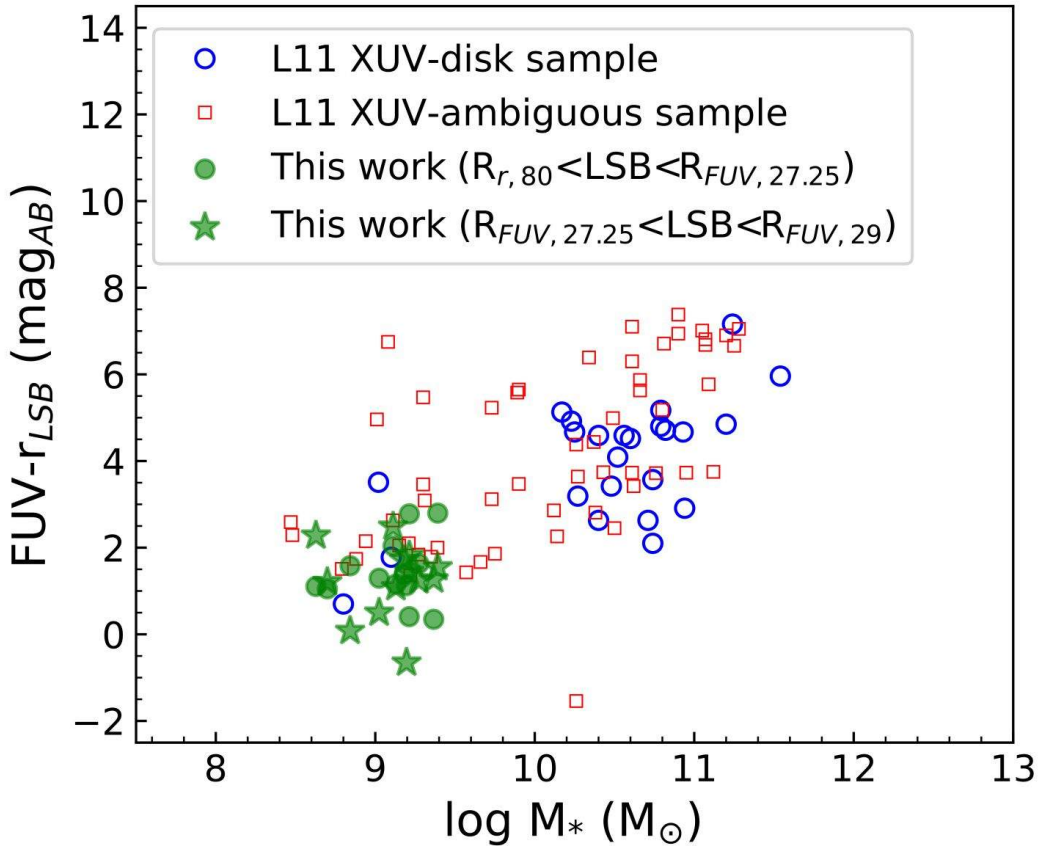

Figure 5.17: **Outer disk FUV-r colour and stellar masses of local BCDs.** Same markers as in Fig. 5.15.

We present a best-case local BCD that satisfy all the criteria we consider for confirming XUV disks in Figure 5.18. This also shows the different diagnostics in our methodology to obtain various properties of the sample.

BCD	$\Delta L_{x,FUV}$	$\Delta L_{x,r}$	FUV-r$_{galaxy}$	FUV-r$_{LSB}$	FUV-r$_{LSB}{}'$	R$_{D,FUV}$	R$_{D,g}$	R$_{D,r}$	R$_{D,z}$	∇(FUV-r)
			mag	mag	mag	kpc	kpc	kpc	kpc	
LBCD01-1	0.19	0.13	1.74	1.16	1.09	0.98	0.98	0.88	0.88	-0.23
***#LBCD01-2**	0.09	0.12	2.49	2.80	1.55	3.14	2.34	2.41	2.05	-0.17
LBCD01-3	<0	<0	2.26	- -	5.23	0.37	0.98	0.98	1.01	0.60
LBCD01-4	0	0	1.88	- -	3.12	0.56	0.89	0.80	0.86	0.42
LBCD01-5	0.35	0.23	0.55	0.41	1.44	1.01	1.02	1.11	1.35	0.00
LBCD02-1	0	0	2.17	- -	2.50	0.89	1.04	1.03	0.80	-0.42
***#†LBCD02-2**	0.23	0.14	1.82	1.12	-0.65	1.05	0.71	0.69	0.64	-1.08
LBCD02-3	<0	<0	2.56	- -	3.07	0.86	0.96	1.03	0.94	0.51
***#†LBCD02-4**	0.22	0.11	2.07	1.29	0.50	0.84	0.66	0.60	0.61	-0.98
LBCD03-1	0	0	2.08	- -	2.22	0.49	0.51	0.52	0.54	0.06
LBCD03-2	1.03	0.14	0.44	0.34	1.27	1.21	1.52	1.63	1.59	-0.52
LBCD03-3	0	0	2.71	- -	3.16	1.09	1.23	1.26	1.30	0.44
LBCD03-5	0	0	1.68	- -	3.20	1.06	1.34	1.28	1.35	-0.20
LBCD03-6	0.13	0.10	2.41	2.04	2.49	0.96	1.09	1.04	1.05	-0.61
LBCD06-1	0	0	2.60	- -	3.79	0.40	0.58	0.60	0.59	0.22
***#LBCD06-3**	0.06	0.10	2.34	2.82	1.83	1.22	0.95	1.02	1.10	0.38
LBCD06-4	0.16	0.17	0.99	1.10	2.28	0.78	1.08	1.21	1.47	-0.06
***#†LBCD07-1**	0.26	0.17	2.11	1.58	0.08	1.45	0.91	0.88	0.81	-0.58
LBCD07-2	0.11	0.08	1.78	1.39	1.69	0.98	1.02	1.00	0.74	-0.66
LBCD08-1	0	0	1.59	- -	2.55	0.73	0.82	0.83	0.83	0.25
LBCD08-2	0	0	2.08	- -	1.96	0.55	0.51	0.56	0.58	-0.09
LBCD08-3	<0	<0	2.56	- -	4.67	0.54	0.84	0.87	0.93	0.44
***LBCD08-4**	0.11	0.09	1.19	1.05	1.21	0.64	0.60	0.59	0.63	-0.06
***#†LBCD09-1**	0.27	0.20	2.03	1.63	1.27	2.09	1.60	1.72	1.39	-0.41
LBCD09-2	0	0	2.45	- -	2.61	0.71	0.65	0.75	0.66	0.31

Table 5.3: **Parameters of the BCDs to assess their XUV nature. Column 2:** FUV light fraction in the LSB region. **Column 3:** r-band light fraction in the LSB region. **Column 4:** FUV-r colour of the whole galaxy. **Column 5**: FUV-r colour in the LSB region. **Column 6:** FUV-r colour in the LSB region within 27.25 and 29 mag arcsec^{-2} FUV surface brightness levels. **Column 7-10:** FUV, g, r and z-band outer disk scale-lengths respectively. **Column 11:** Overall FUV-r gradient of the galaxy.

* marks those BCDs which have $\Delta L_{x,FUV} > 0$ and R$_{D,FUV}$ > R$_{D,g}$.

marks those BCDs which have FUV-r$_{galaxy}$ >FUV-r$_{LSB}{}'$ and R$_{D,FUV}$ >R$_{D,grz}$.

† marks those BCDs which have $\Delta L_{x,FUV} > \Delta L_{x,r}$, FUV-r$_{galaxy}$ > FUV-r$_{LSB}$ (and FUV-r$_{LSB}{}'$), R$_{D,FUV}$ >R$_{D,grz}$ and ∇(FUV-r)<0.

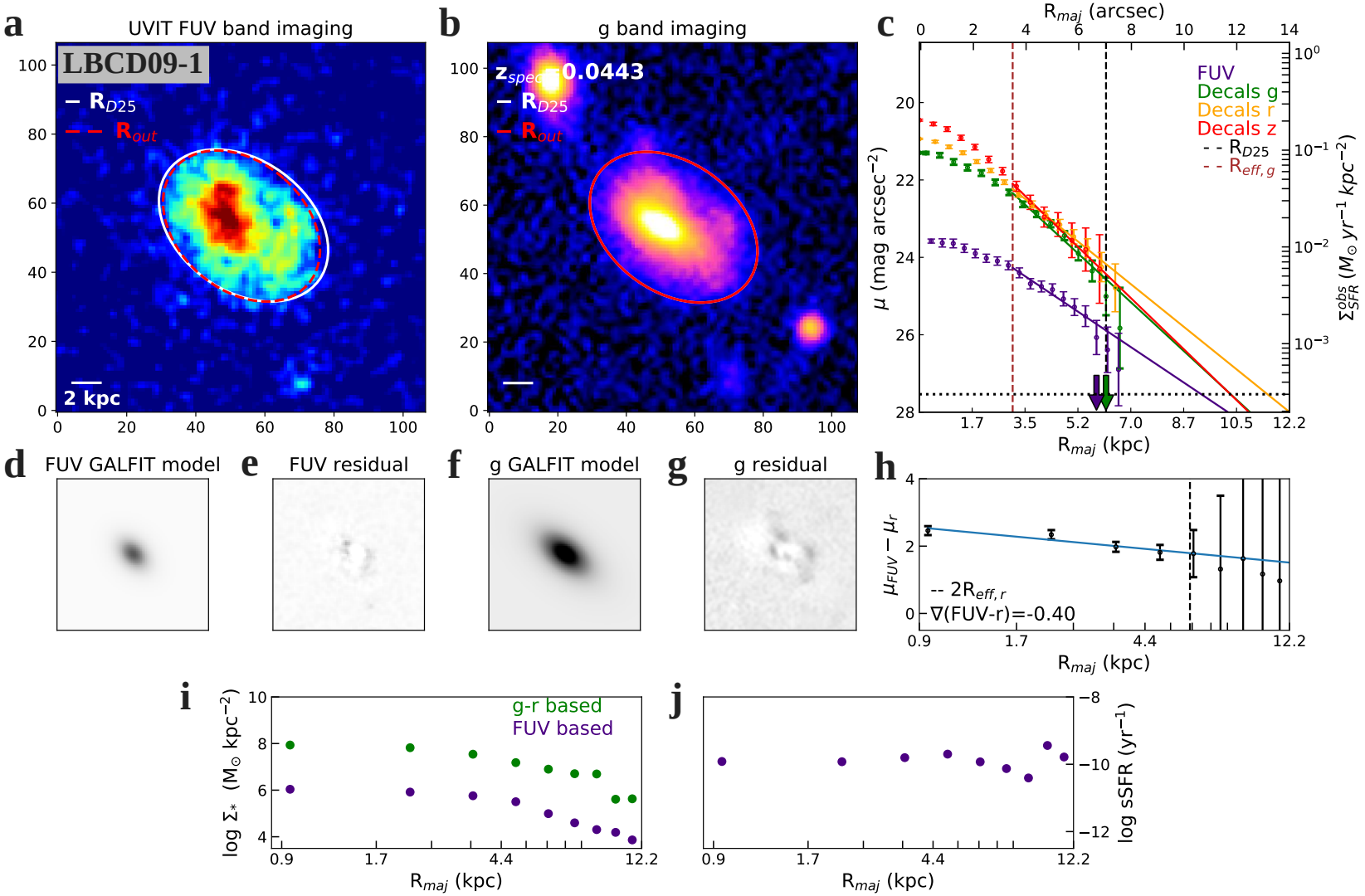

Figure 5.18: **Different structural parameters of a sample local BCD. a,b**: Shows the imaging of a sample BCD (LBCD09-1) in the *UVIT* FUV and DECaLS g-band. The cutouts are of the size 4 times the $R_{eff,g}$. **c**: The surface brightness profiles of the BCD in 4-bands. The S/N = 3 extents are marked by red dashed ellipses in the case of FUV and solid red ellipses in the case of g-band in **a** and **b**. These are marked by indigo and green upside-down arrows in **c**. The R_{25} extent is shown as white ellipses in the case of the imaging data (**a,b**) and as a vertical dashed black line in the combined surface brightness plot (**c**). **d,e,f,g**: 2D GALFIT models and residuals in the FUV and g-bands. **h**: FUV-r radial colour plot with a linear fit to obtain the overall FUV-r gradient in the galaxy. The optical as well FUV imaging show clumpy morphologies. **i,j**: Stellar mass surface density and sSFR profiles. The sSFR profile shows a mild increased sSFR in the outer parts. All errors are 1σ.

5.5 Summary and Conclusions

In this chapter, we present our new *AstroSat/UVIT* FUV observations for a sample of 25 nearby BCDs at z∼0.03. We acquire multi-wavelength observations additionally from the DESI Legacy survey in the g,r and z bands. We perform multi-wavelength structural analysis in 1D as well in 2D (to first order). Our objective is to look for XUV emission in nearby BCDs and understand their mass assembly history. Our 2D single Sersic models reveal that the nearby BCDs are disky in the optical but show both disky and cored morphology in the FUV. At the same time, the half-light radii are similar to or smaller in the FUV as compared to their optical counterparts. Detailed structural decomposition of the BCDs is kept for a future work. The 1D profiles also reveal that the S/N = 3 sizes of the BCDs in FUV are mostly smaller than in the optical bands. We obtain the scale-length of the outer disk of these BCDs across FUV and optical bands. We find that 7 out of 25 BCDs have FUV scale-lengths larger than the optical which indicates younger stars at farther distances. The BCDs may be spatially extended in the FUV but we cannot confirm this due to the current depth of the observations. We estimate the outer disk UV-optical colours and FUV, optical light fraction which reveal that at least 4 (and at most 6) of the BCDs with larger FUV scale-lengths also have younger stars in the outer parts as compared to the overall galaxy population. These 4 BCDs also have outer FUV light fraction greater than that in the r-band. Incidentally, the overall FUV-r gradient of the BCDs is also negative for 6 of them. Our results indicate the presence of XUV disks in 16-24% of the studied sample of BCDs. We do not try to classify these BCDs as Type 1 or Type 2 XUV as per T07 because we cannot make a direct one-to-one comparison as explained earlier in this chapter. We can expect our XUV disk BCDs to be similar to Type 2 XUV disks in T07 but it remains uncertain with the present observations. We also assess the mass assembly history by studying the sSFR variation over the galaxy. We find that there are individual cases where sSFR increases outwards, likely indicating an inside-out assembly mode. However, the average sSFR profile of the complete BCD sample remains essentially flat which likely implies that the local BCD disks have assembled in

a self-similar way throughout. However, there is also the possibility that most of these BCDs have come beyond their XUV phases which could be episodic. This should give the BCDs enough time to produce flattened sSFR profiles until there is another trigger for XUV disk star formation.

Appendix

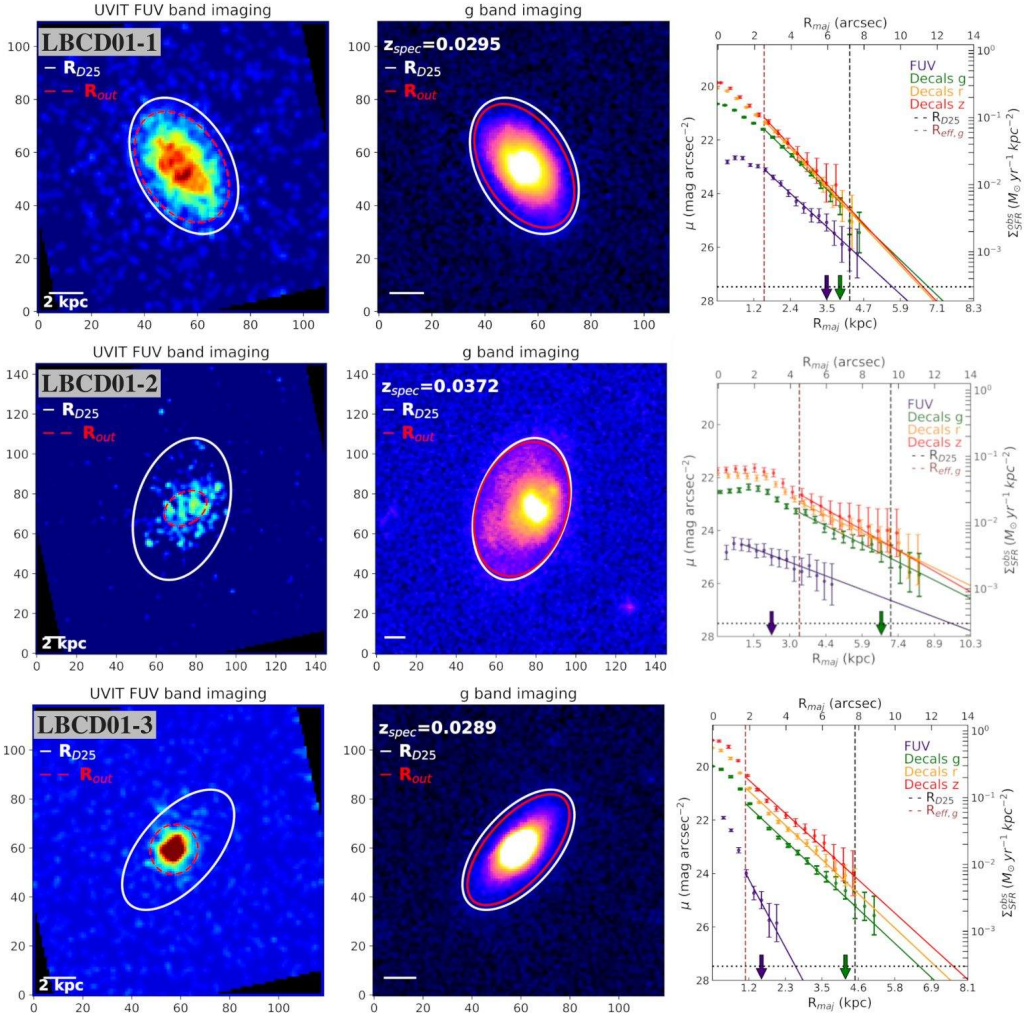

Figure 5.19: BCD false color imaging in the *UVIT* FUV (left) and DECaLS g-band (middle). The cutouts are of the size 4 times the $R_{eff,g}$. The S/N = 3 extents are marked by red dashed ellipse in case of FUV and solid red ellipse in case of g-band. The R_{25} extent is shown by white ellipses. Right: The surface brightness profile of the BCDs in 4-bands. The S/N = 3 extents are marked by indigo and green upside down arrows. The R_{25} extent is shown as a vertical dashed black line. All error-bars represent 1σ errors.

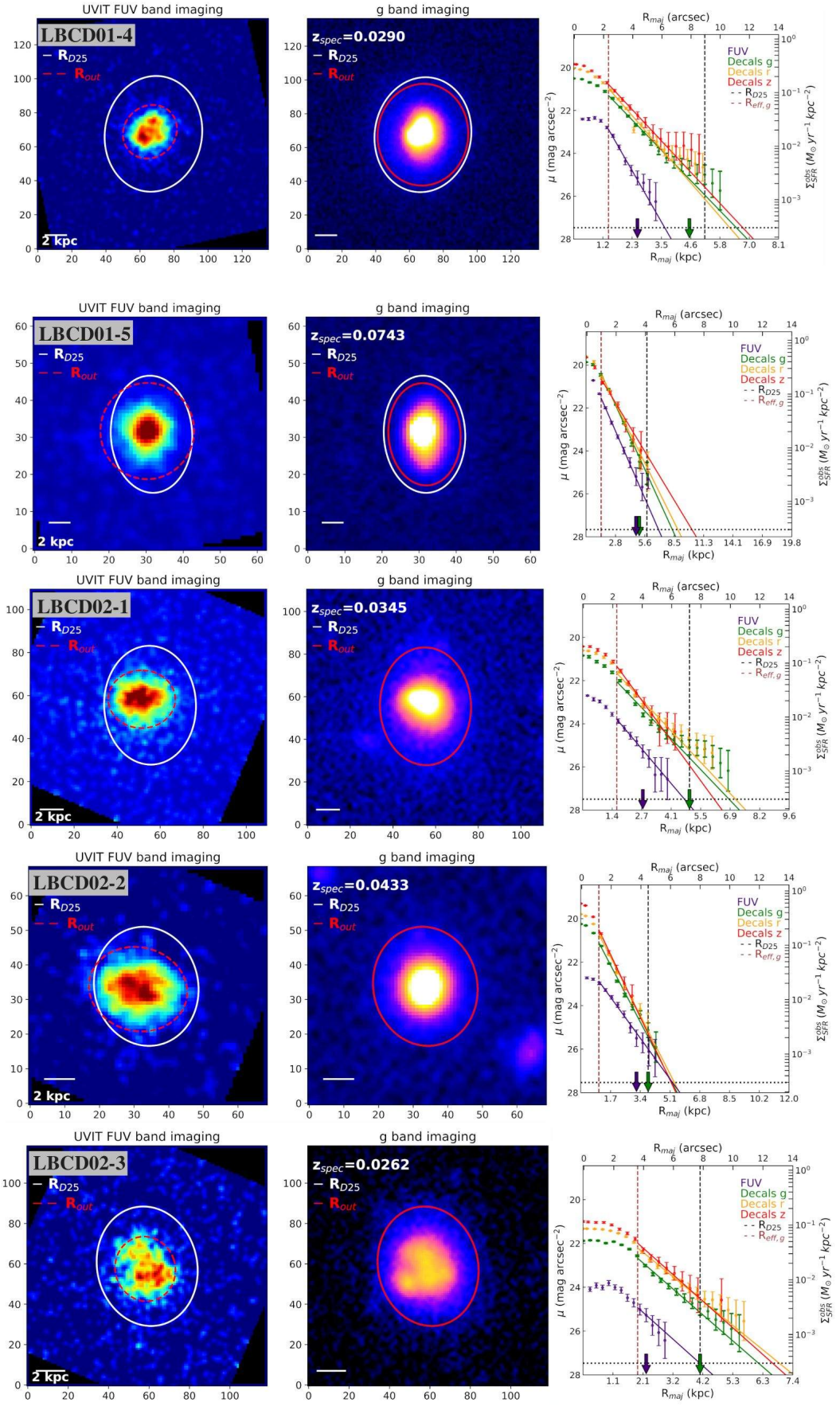

Figure 5.20: Same as Figure 5.19.

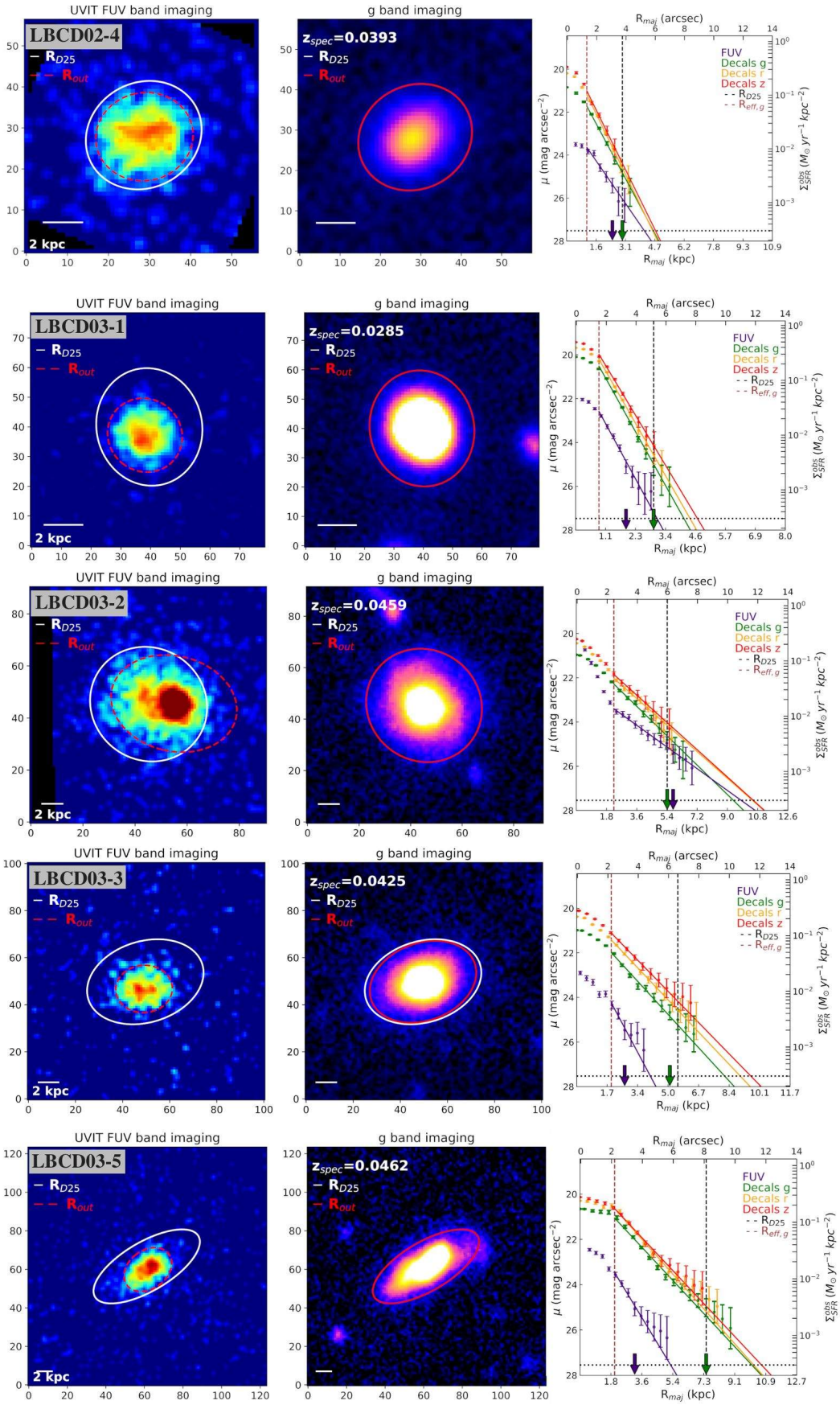

Figure 5.21: Same as Figure 5.19.

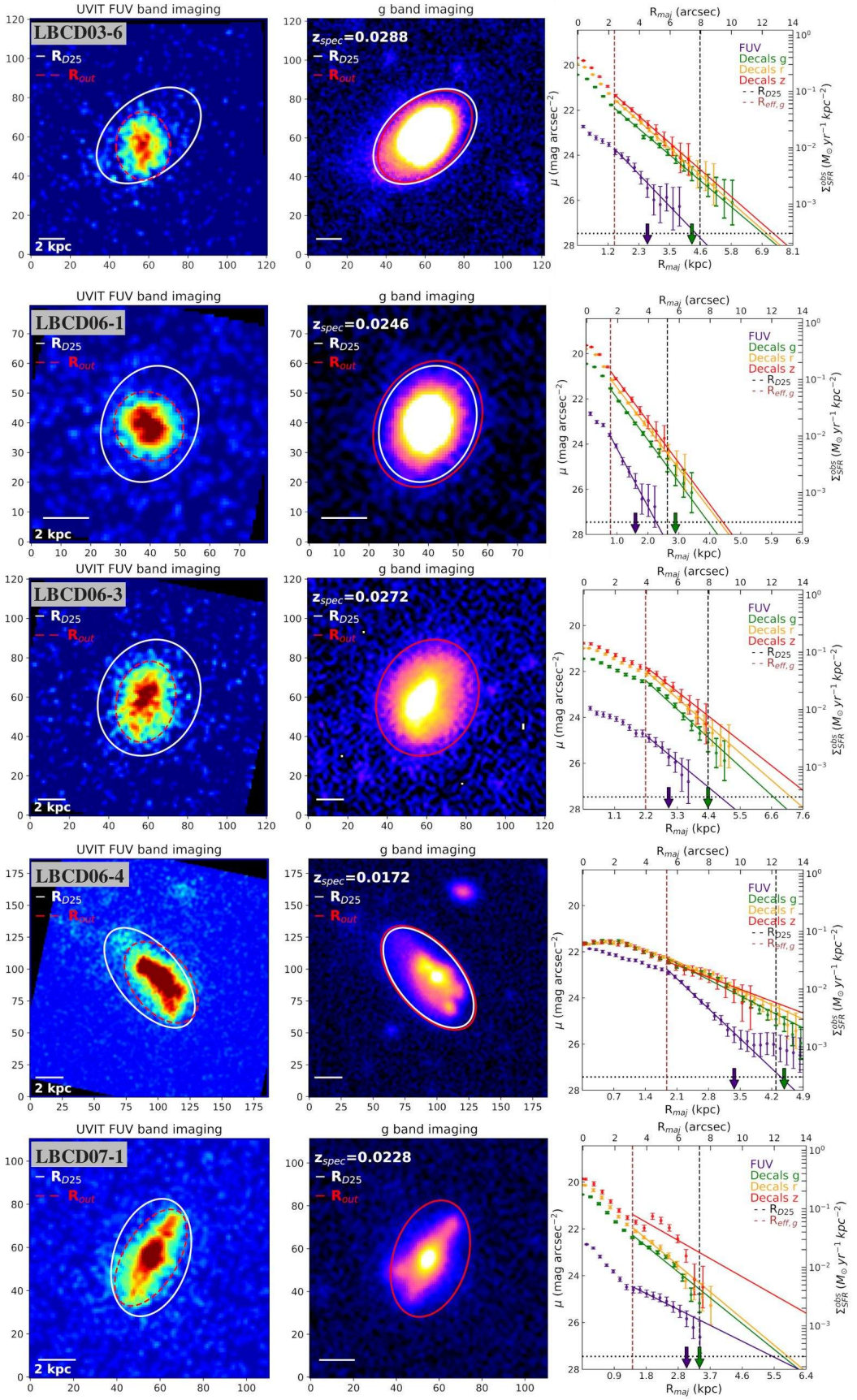

Figure 5.22: Same as Figure 5.19.

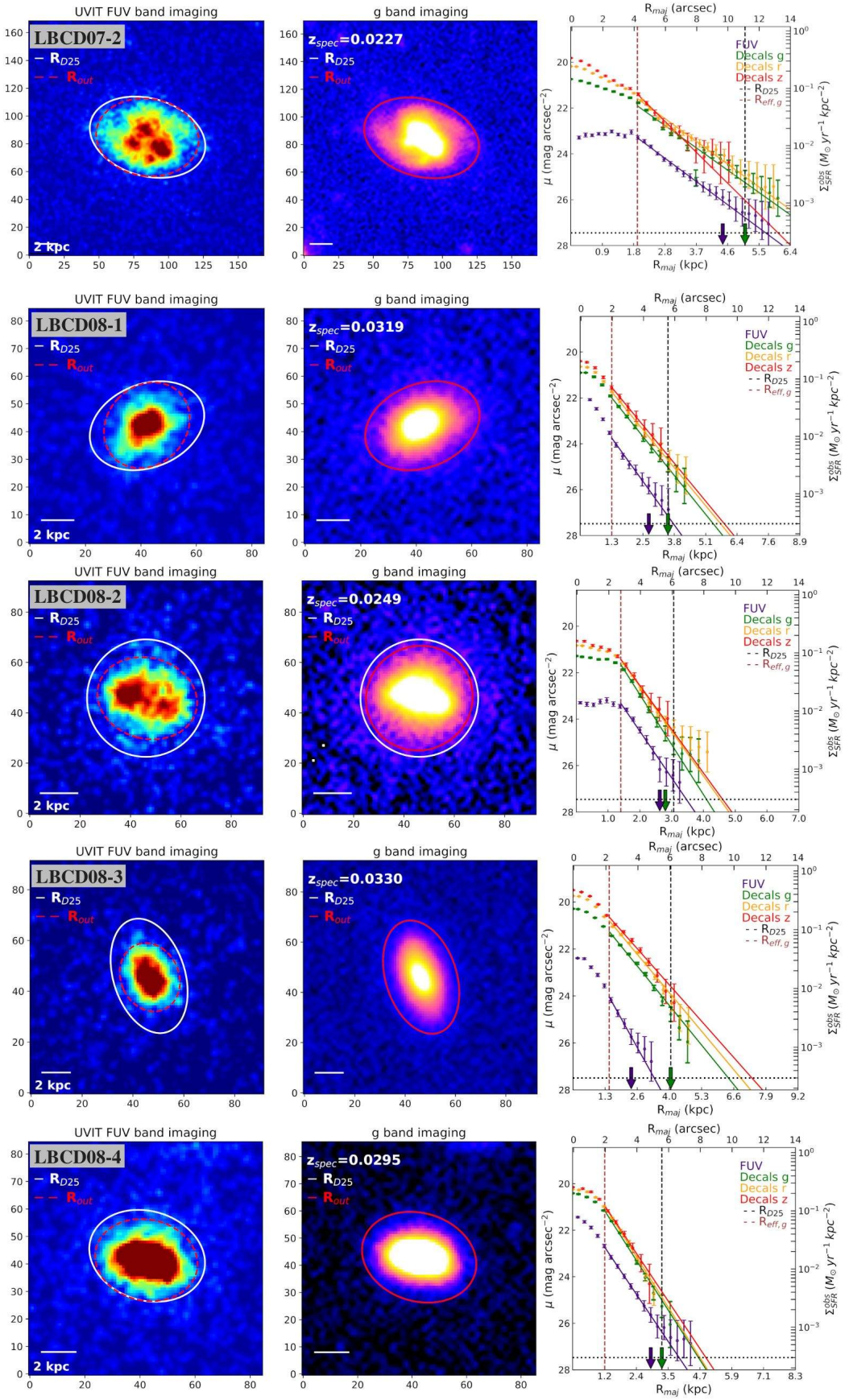

Figure 5.23: Same as Figure 5.19.

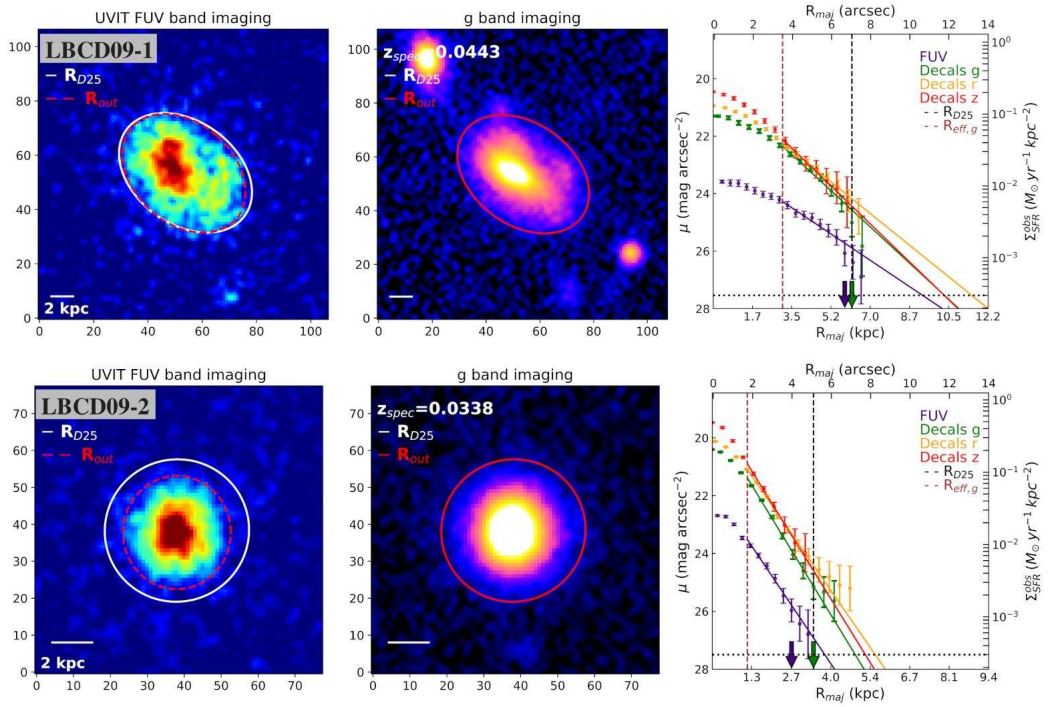

Figure 5.24: Same as Figure 5.19.